Article

Current Biology

Competition for Space Induces Cell Elimination through Compaction-Driven ERK Downregulation

Graphical Abstract

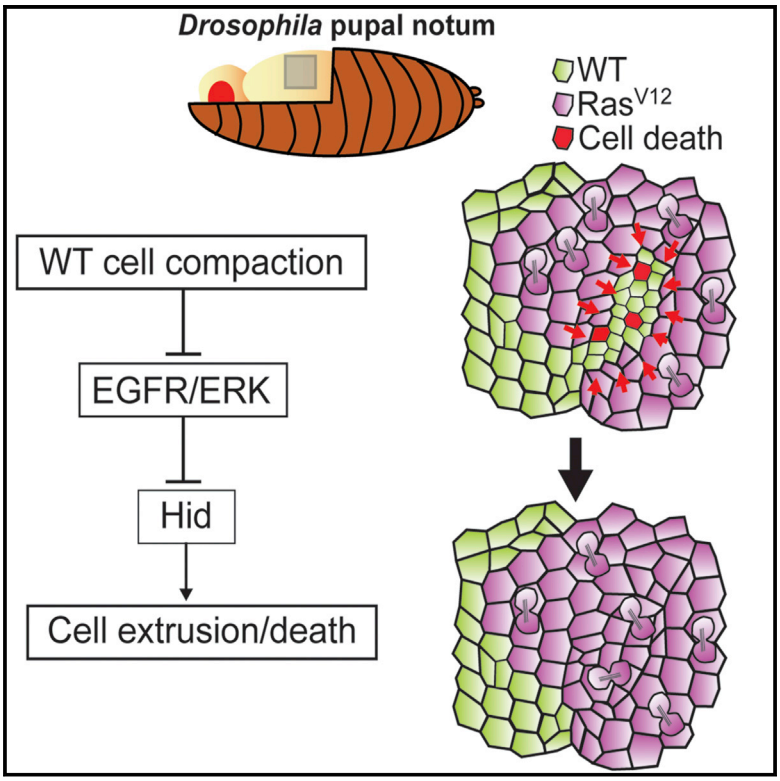

Authors

Eduardo Moreno, Léo Valon, Florence Levillayer, Romain Levayer

Correspondence

eduardo.moreno@research.fchampalimaud.org (E.M.), romain.levayer@pasteur.fr (R.L.)

In Brief

Moreno et al. show that cell elimination in the *Drosophila* pupal notum can be locally adjusted by tissue deformation through the modulation of EGFR/ERK pathway and the pro-apoptotic gene *hid*. Compaction-driven ERK downregulation also occurs near fast-growing clones and promotes clone expansion through neighboring cell elimination.

Highlights

- Caspase activity in *Drosophila* pupal notum is regulated by EGFR/ERK and *hid*
- EGFR/ERK can be activated or downregulated by tissue stretching or compaction
- Cell compaction near fast-growing clones downregulates ERK and triggers cell death
- Compaction-driven ERK downregulation promotes fast-growing clone expansion

Moreno et al., 2019, Current Biology *29*, 23–34
January 7, 2019
https://doi.org/10.1016/j.cub.2018.11.007

CellPress

Current Biology
Article

Competition for Space Induces Cell Elimination through Compaction-Driven ERK Downregulation

Eduardo Moreno,[1,*] Léo Valon,[2] Florence Levillayer,[2] and Romain Levayer[2,3,*]
[1]Champalimaud Centre for the Unknown, Av. Brasília, 1400-038 Lisbon, Portugal
[2]Department of Developmental and Stem Cell Biology, Institut Pasteur, 25 rue du Dr. Roux, 75015 Paris, France
[3]Lead Contact
*Correspondence: eduardo.moreno@research.fchampalimaud.org (E.M.), romain.levayer@pasteur.fr (R.L.)
https://doi.org/10.1016/j.cub.2018.11.007

SUMMARY

The plasticity of developing tissues relies on the adjustment of cell survival and growth rate to environmental cues. This includes the effect of mechanical cues on cell survival. Accordingly, compaction of an epithelium can lead to cell extrusion and cell death. This process was proposed to contribute to tissue homeostasis but also to facilitate the expansion of pretumoral cells through the compaction and elimination of the neighboring healthy cells. However, we know very little about the pathways that can trigger apoptosis upon tissue deformation, and the contribution of compaction-driven death to clone expansion has never been assessed *in vivo*. Using the *Drosophila* pupal notum and a new live sensor of ERK, we show first that tissue compaction induces cell elimination through the downregulation of epidermal growth factor receptor/extracellular signal regulated kinase (EGFR/ERK) pathway and the upregulation of the pro-apoptotic protein Hid. Those results suggest that the sensitivity of EGFR/ERK pathway to mechanics could play a more general role in the fine tuning of cell elimination during morphogenesis and tissue homeostasis. Second, we assessed *in vivo* the contribution of compaction-driven death to pretumoral cell expansion. We found that the activation of the oncogene Ras in clones can downregulate ERK and activate apoptosis in the neighboring cells through their compaction, which eventually contributes to Ras clone expansion. The mechanical modulation of EGFR/ERK during growth-mediated competition for space may contribute to tumor progression.

INTRODUCTION

Developing tissues can cope with perturbations, including stress from the environment or abnormal behaviors of a subset of cells. This robustness relies on the plasticity of cell behavior and/or fate, which can adjust to changes in the tissue environment. Modulation of cell proliferation and cell death can be driven by contact-dependent communication, extracellular diffusive factors, and/or mechanical inputs [1]. Accordingly, mechanical cues have been proposed to adjust the local rate of cell death and cell division to regulate tissue final size or to maintain it during homeostasis [2–4].

The regulation of cell death by mechanical inputs is well documented in epithelia. Epithelial compaction can induce cell extrusion and cell death in MDCK cells, zebrafish epidermis [5–7], and in the midline region of the *Drosophila* pupal notum (a single layer epithelium; Figure 1A) [8]. Recently, we showed that compaction-driven cell elimination in the pupal notum relies on caspase activation, which is required for and precedes every extrusion event [9]. Thus, some pathways must be sensitive to tissue deformations and trigger and/or modulate caspase activation. However, we could not find a clear contribution of known mechanosensitive pathways to midline cell elimination, including p53 [7], the JNK pathway [10], or the Hippo Yap/Taz pathway [9, 11]. Moreover, it also suggested that cells could have differential sensitivity to compaction depending on their sensitivity to apoptosis. Accordingly, activation of Ras in clones led to the preferential compaction and elimination of the neighboring wild-type (WT) cells [9]. Similarly, the high levels of p53 in mutant MDCK cells for the polarity gene *scribble* increase their sensitivity to compaction and trigger their elimination when surrounded by WT MDCK cells [7, 12]. Those eliminations have been proposed to promote the expansion of pretumoral cells through a so-called mechanical cell competition [7, 9, 13, 14]. However, the molecular pathway triggering cell death during mechanical cell competition *in vivo* was not yet identified, and it was not yet clear whether such elimination could significantly promote pretumoral clone expansion.

Here, we show that tissue compaction induces cell elimination in the pupal notum through the downregulation of epidermal growth factor receptor/extracellular signal regulated kinase (EGFR/ERK) pathway and the upregulation of the pro-apoptotic protein Hid (head involution defective). Using a new *Drosophila* live sensor of ERK activity, we demonstrate that local tissue stretching or compaction transiently upregulate or downregulate ERK activity, hence increasing or decreasing cell survival. Moreover, we show that compaction-driven ERK downregulation near Ras-activated clones controls cell elimination and promotes clone expansion. The sensitivity of EGFR/ERK pathway to mechanics and its role in the fine tuning of cell elimination could play a more general role during tissue homeostasis and tumor progression.

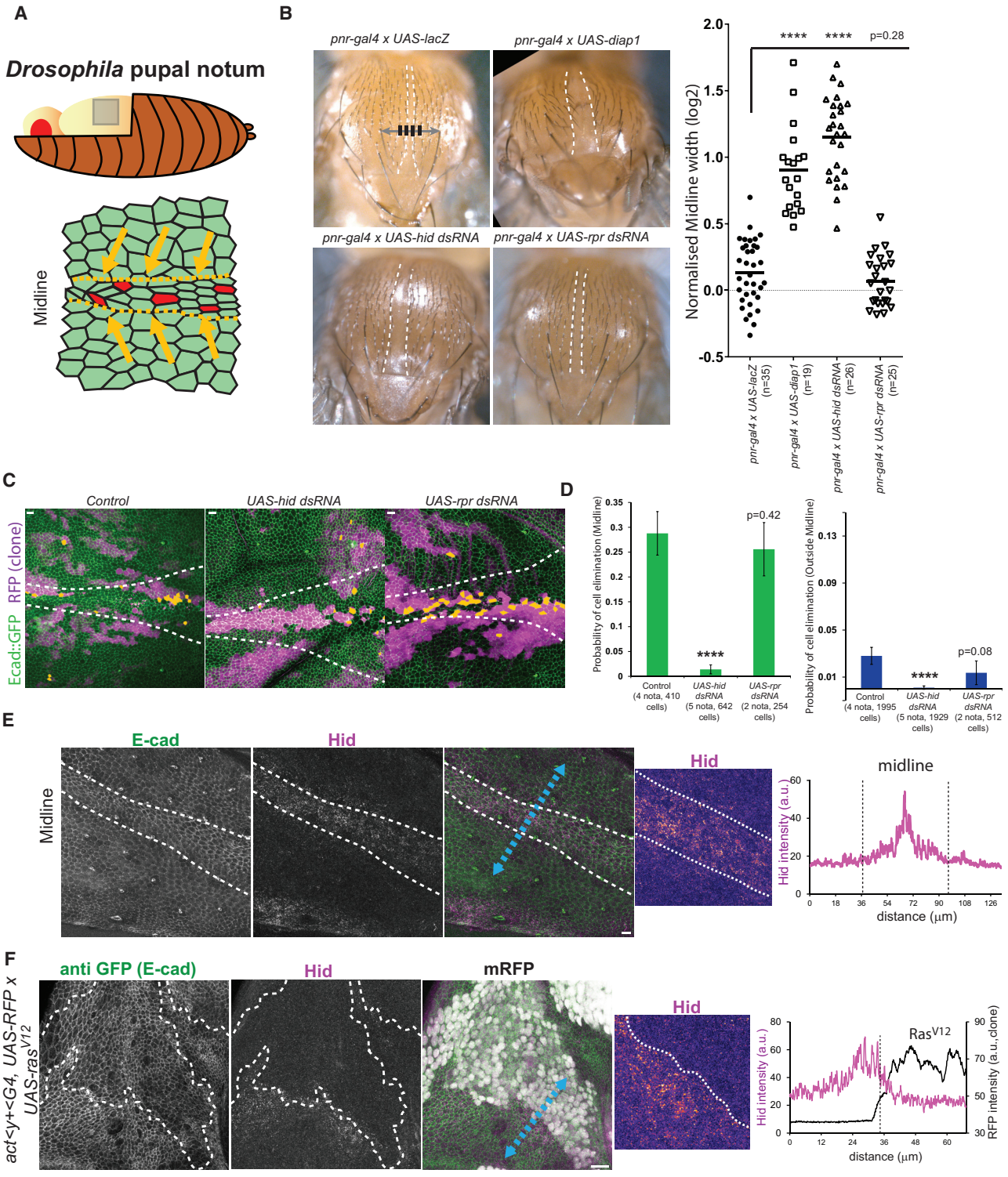

Figure 1. Hid Is Required for Cell Elimination

(A) Schematic of the pupal notum and the midline (bottom). Orange arrows, compaction; red cells, caspase-activated cells.

(B) Adult thorax upon perturbation of cell death in the *pnr* domain. White dashed lines, midline. Black lines are used to measure the relative midline width (see STAR Methods). Right graph: normalized midline width is shown (log2 scale; one point = 1 thorax); t test with control; ****$p < 10^{-4}$.

(C) Live pupal nota expressing *ubi-Ecad::GFP* (green) with Gal4-expressing clones (RFP, magenta) in controls (ayG4 alone) or expressing *UAS-hid dsRNA* or *UAS-rpr dsRNA* (white dashed lines: midline). Orange cells: clonal cells that will die. Scale bars represent 10 μm.

(legend continued on next page)

RESULTS

Cell Elimination in the Pupal Notum Is Regulated by Hid

We previously showed that a deletion covering the three pro-apoptotic genes *hid*, *grim*, and *reaper* (*H99* deletion) strongly downregulated cell extrusion in the pupal notum [9]. Downregulation of *hid* by RNAi in the pupal notum (using *pnr-gal4* driver) led to a significant widening of the midline in the adult fly thorax (a zone with a high rate of cell elimination) [8, 9, 15], similar to apoptosis downregulation through *diap1* overexpression (Figure 1B). Moreover, downregulation of *hid* in clones strongly reduced their rate of cell extrusion inside or outside the midline (Figures 1C and 1D; Video S1), phenocopying the defects observed with the *H99* deletion [9]. Accordingly, *rpr* downregulation had no significant effect on thorax morphology and clone survival (Figures 1B–1D; Video S1). Thus, *hid* must be responsible for the defects observed in *H99* deletion. Finally, Hid protein also accumulated in regions showing a high rate of cell elimination, including the midline (Figure 1E) and in crowded regions near Ras^{V12} clones (Figure 1F). Altogether, this suggests that Hid is a central regulator of cell death in the pupal notum and that it can be upregulated in crowded regions.

Cell Survival in the Midline Is Regulated by EGFR/Ras/Raf/ERK Pathway

We next tried to identify the regulators of Hid in the midline of the notum. Hid can be upregulated by the steroid hormone ecdysone [16], downregulated by the pro-survival microRNA bantam [17], and downregulated by the EGFR/Ras/Raf/ERK pathway [18, 19]. There was no accumulation of ecdysone receptor (Figure S1A) or a downregulation of bantam in the midline (Figure S1B). Moreover, overexpression of a Bantam sponge in clones (which sequesters bantam microRNA [17] and reduces bantam activity; Figure S1C) did not affect cell elimination (Figures S1D and S1E; Video S1). Thus, ecdysone and bantam are not responsible for the upregulation of Hid in the midline. Interestingly, we observed a relative downregulation of ERK activity in the midline (Figures S1F and 2A). As such, we tried to identify the upstream signal regulating ERK activity in the midline. EGFR downregulation led to a narrowing of the *pnr* domain in the adult thorax (Figure 2B), which could be rescued by downregulation of *hid* (Figure 2B). Therefore, EGFR is required for cell survival in the pupal notum through *hid* downregulation. This effect was specific of EGFR, as we did not observe such narrowing upon Pvr/PDGF, FAK, Src42A, and Src64B downregulation (Figure S2A), other putative regulators of ERK [21–23]. We then tested the impact of EGFR on cell survival in the notum. Downregulation of EGFR in clones led to a strong increase of cell elimination everywhere in the notum, and overexpression of a chimeric EGFR (hEGFR::GFP, which can activate ERK independently of extracellular ligands) [24] nearly abolished cell elimination (Figures 2C and 2D; Video S1; ERK activity shown in Figure 3C). EGFR/Ras could promote cell survival through the phosphatidylinositol 3-kinase (PI3K) pathway or the Raf/mitogen-activated protein kinase (MAPK) pathway [25]. However, activation of PI3K in clones had little impact on the rate of cell elimination (Figure S2B; Video S1) and overexpression of an active form of Raf strongly abolished cell elimination (Figure S2C; Video S1). Altogether, we conclude that EGFR/Ras/Raf/ERK pathway is a central regulator of cell survival in the pupal notum.

Development of a New Live Sensor of ERK

We then asked whether ERK downregulation was playing an instructive role for caspase activation rather than a purely permissive function. To do so, we developed a new live sensor of ERK activity. Phosphorylation of the transcriptional repressor Capicua (Cic) by ERK leads to its removal from the nucleus [20]. We used a minimal domain of Cic lacking its DNA binding domain and containing the phosphorylation and docking site of ERK [20] fused to a nuclear localization sequence (NLS) and mCherry under the control of the *tubulin* promoter (Figure 3A; hereafter named miniCic). We expected to observe a nuclear accumulation of miniCic upon ERK downregulation and an exclusion from the nucleus upon ERK activation. miniCic nuclear intensity was indeed anticorrelated with the endogenous levels of active ERK in the wing and eye imaginal discs (Figure 3B; note the gradient in the eye disc) [26] and in the embryos (Figure S3A) with a clear exclusion from the nucleus in active regions (Figure 3B, right). Thus, miniCic is suitable for quantitative measurements of endogenous levels of ERK activity. MiniCic also accurately reported modulations of EGFR/ERK activity in the pupal notum by expressing EGFR double-stranded RNA (dsRNA) or hEGFR::GFP in clones (Figure 3C). We then assessed the potential time delay between ERK modulation and miniCic relocalization. Inhibition of ERK through the MEK inhibitor trametinib [27] led to rapid disappearance of dpERK in S2 cells (Figure 3D; 5 min after adding drug at 10 μM) and a rapid nuclear accumulation of miniCic in haemocytes (Figure 3E; Video S2A; significant increase 10 min after adding drug). Moreover, the fast induction of dpERK in the lateral ectoderm of cellularizing embryos [28] was also captured by miniCic, except for a short developmental time window of 10–15 min (Figure S3A). Altogether, this showed that miniCic could be used to assess the variations of endogenous ERK activity with a maximum lag time of 10–15 min.

We then used this new sensor to visualize the dynamics of ERK in the pupal notum and check whether it could reflect the pattern of ERK activity we previously described by immunostaining (Figures 2A and S1F). As expected, we observed an accumulation of

(D) Probability of cell elimination in clones in the midline (left) and outside the midline (right). Fisher exact test with the control; ****$p < 10^{-4}$. Error bars indicate 95% confidence interval.

(E) Immunostaining of a pupal notum, z-projection of anti-E-cad (green), and anti-Hid (magenta) in the midline (white dashed line; 7/7 nota). Close-up view of Hid intensity in the midline in pseudocolor is shown in the right panel. Right graph: intensity profile of Hid along the blue dashed line (magenta) is shown. Scale bar represents 10 μm.

(F) Immunostaining of a pupal notum showing z-projection of anti-GFP (E-cad::GFP, green), anti-Hid (magenta), and upstream activating sequence (UAS)-nlsRFP signal (white) in vicinity of a clone where Ras was conditionally activated (*UAS-ras*^{V12}; 24 hr activation at 29°C; white dashed lines: clone boundaries); 4/4 nota. Right: close up view of Hid intensity near the clone in pseudocolor is shown. Right graph: intensity profile of Hid along the blue dashed line (magenta) and RFP (clone, black line) is shown. Scale bar indicates 10 μm.

See also Video S1 and STAR Methods.

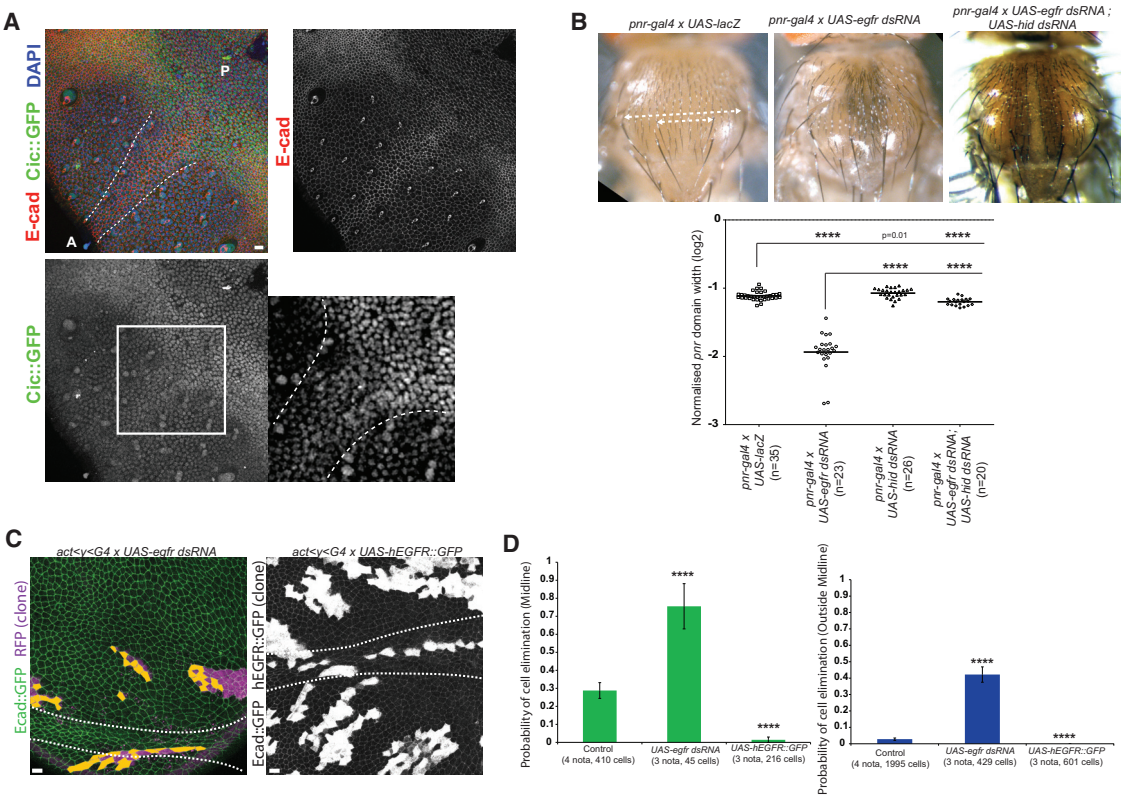

Figure 2. EGFR/ERK Downregulation Is Necessary and Sufficient for Cell Elimination

(A) Anti-E-cad (red), DAPI (blue), and anti-GFP (*cic-Cic::GFP*, BAC clone, green, negatively regulated by ERK) [20] in the midline (white dashed line; 7/7 nota); higher magnification shown on the right (white square region). 5/5 nota are shown. Scale bar represents 10 μm. A, anterior; P, posterior.

(B) Adult thorax in control (*pnr-gal4* × *UAS-lacZ*) upon EGFR downregulation (*pnr-gal4* × *UAS-EGFR dsRNA*) and downregulation of EGFR and Hid (*pnr-gal4* × *UAS-EGFR dsRNA; UAS-hid dsRNA*). White dashed lines: *pnr* domain width and total thorax width (see STAR Methods). (Bottom graph) Normalized *pnr* domain width is shown (log2 scale; one point = 1 thorax); t tests; ****$p < 10^{-4}$.

(C) Live pupal nota expressing *ubi-Ecad::GFP* (green) with Gal4-expressing clones where EGFR is downregulated (*UAS-egfr dsRNA*, left; clones in magenta) or upregulated (*UAS-hEGFR::GFP*; *H. sapiens* extracellular domain and *Drosophila* intracellular domain; clones marked in white). White dashed lines: midline. Orange cells: clonal cells that will die. See Figure 1C for control. Scale bars represent 10 μm.

(D) Probability of cell elimination in the clones in the midline (top) and outside the midline (bottom). Fisher exact test with the control condition (same as Figures 1C and 1D); ****$p < 10^{-4}$. Error bars indicate 95% confidence interval.

See also Figures S1 and S2, Video S1, and STAR Methods.

miniCic (low ERK activity) mostly in the midline and in an orthogonal domain in the posterior part of the notum (Figure 3F; Video S2B), both corresponding to zones of high cell death rate (Figure 3F) [9, 15]. The local dynamics of miniCic correlated with the temporal and spatial distribution of cell elimination, which occurred first mostly in the midline and then in the posterior region (Figures S3B–S3D; Video S2B). This suggested again that ERK dynamics and levels correlated with cell death distribution in the notum.

Reduction of ERK Activity Precedes Caspase Activation

We then checked whether ERK downregulation preceded the activation of caspases at the single-cell level in the midline. Using the fluorescence resonance energy transfer (FRET) caspase sensor Scat3 [29] combined with miniCic, we systematically detected the onset of caspase activation in single cells and measured nuclear miniCic before and after caspase activation. A significant downregulation of ERK signaling preceded the onset of caspase activation for up to 1 hr (Figures 4A–4C; Video S2C), and ERK was slightly upregulated in cells that did not activate caspases (Figure 4C, gray curve; coherent with the global activation observed in Video S2B). Accordingly, 61% of the caspase-activating cells showed an unambiguous increase of miniCic during the last hour preceding caspase activation (n = 165 cells, 2 pupae). Those data confirm at the single-cell level the instructive role of ERK downregulation on caspase activation. However, it also suggests that unknown factors may also trigger caspase activation in the notum.

ERK Can Be Ectopically Activated or Downregulated by Tissue Stretching or Compaction

Cell death in the pupal notum can be downregulated by tissue stretching and ectopically induced by tissue compaction [9]. Because EGFR/ERK is a central regulator of notum cell death, we tested whether ERK activity could be modulated by tissue deformations. Using particle image velocimetry (PIV) to measure local tissue deformations [9], we first compared the local rate of deformation in unperturbed nota with local variations of miniCic

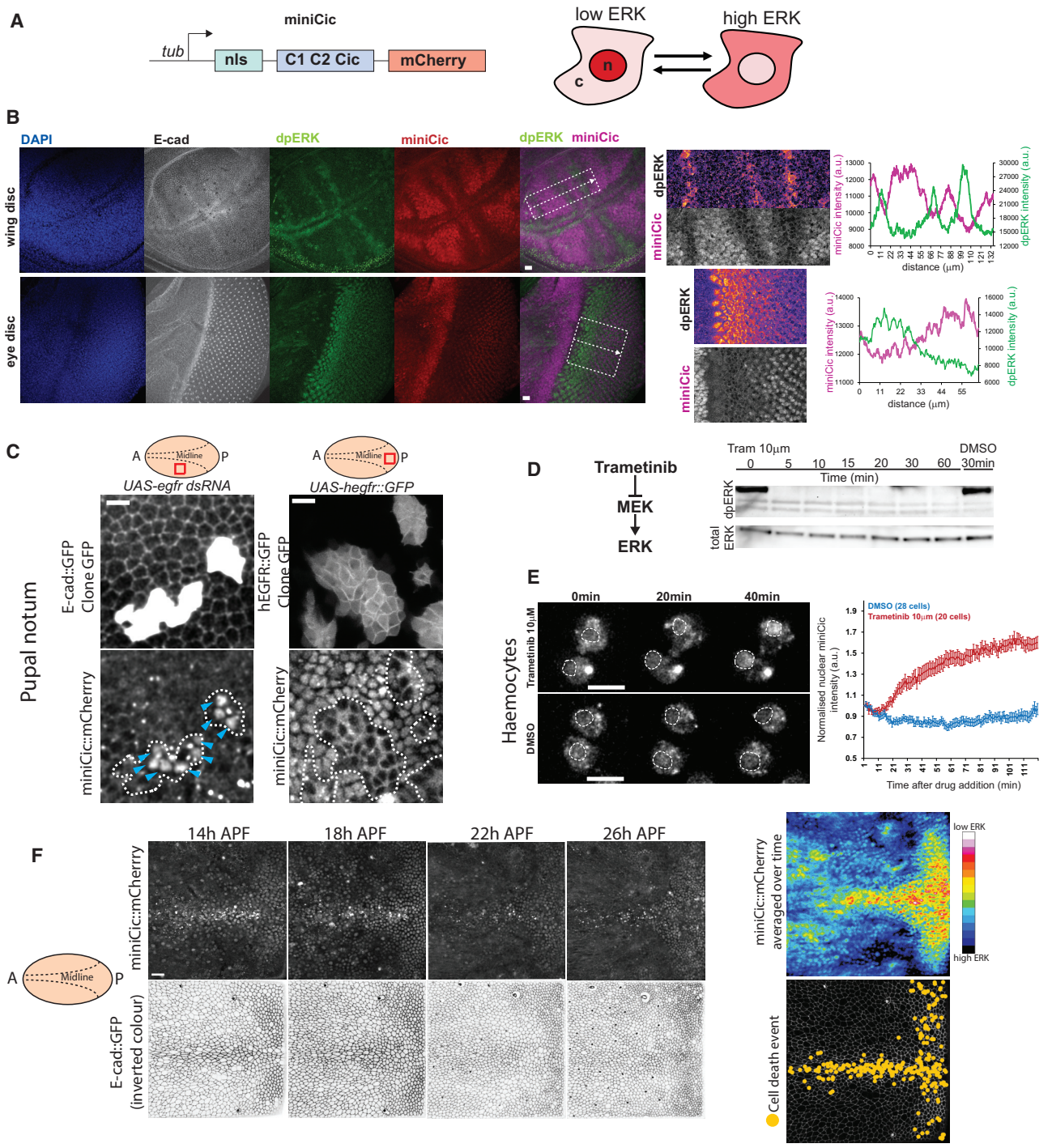

Figure 3. A New Live Sensor of ERK

(A) Schematic of the miniCic construct. Right cartoon: expected localization of miniCic at low ERK activity (accumulation in nucleus, n) and high ERK activity (exclusion in the cytoplasm, c) is shown.

(B) z-projection of immunostainings of a wing imaginal disc (top) and an eye imaginal disc (bottom) at the L3 wandering stage (10/10 tissues for each) stained for DAPI (blue), E-cad (white), dpERK (green), and miniCic (anti-mCherry, red; purple on the overlay). Scale bars represent 10 μm. Close-up views (dashed white rectangles) are shown on the right (single plane; dpERK pseudocolor; miniCic greyscale); graphs: intensity line profiles of dpERK (green) and miniCic (purple) along white dashed rectangles.

(C) Live pupal nota expressing miniCic and endo-Ecad::GFP with EGFR-depleted clones (left, green GFP; *UAS-egfr dsRNA*) or clones overexpressing hEGFR (right, *UAS-hegfr::GFP*). Top schemes: localization of the clones in the notum is shown (red rectangles; A, anterior; P, posterior; dashed lines, midline; zone of high

(legend continued on next page)

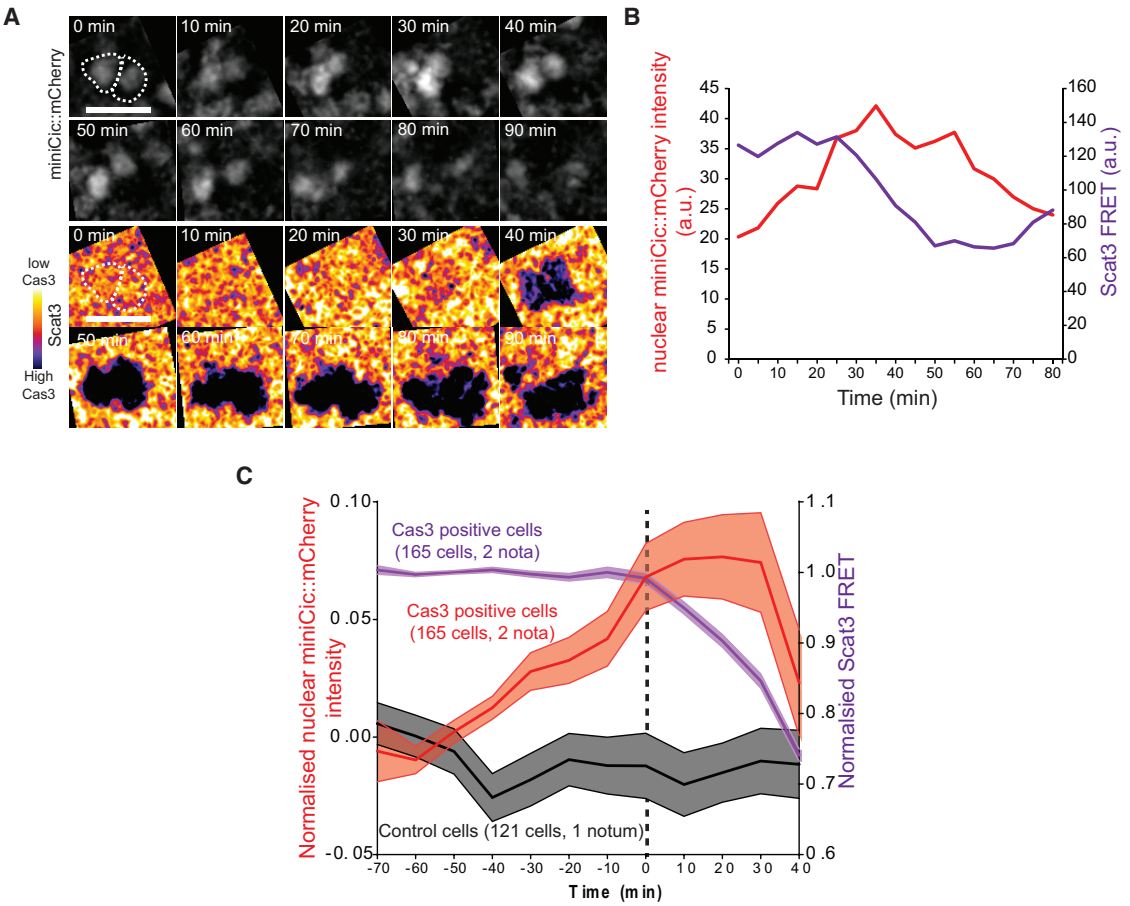

Figure 4. ERK Downregulation Precedes Caspase Activation

(A) Snapshots of two nuclei in the midline of the pupal notum showing miniCic signal (top) and Scat3 FRET signal (bottom; dark blue signal, caspase activation). Scale bars represent 10 μm.

(B) miniCic nuclear signal of the left nucleus shown in (A) (red) and FRET signal (purple).

(C) Averaged normalized profiles of miniCic nuclear intensity (red) in the midline aligned at t0 = onset of caspase activation (maximum inflexion of the FRET signal). Light colored areas are ± SEM. The averaged Scat3 FRET signal is shown in purple. Grey curve: normalized averaged miniCic signal of midline cells that do no activate caspase.

See also Video S2.

signal. We found a good correlation between local tissue stretching (Figure 5A, bottom left) and local activation of ERK activity, especially in the posterior region of the notum, where we observed a global stretch orthogonal to the antero-posterior (AP) axis around 20 hr after pupal formation (APF) (Figures 5A and 5B; Videos S2B and S3). This was reflected by the significant positive cross-correlation between miniCic signal derivative and the compaction rate (Figures 5B and 5C; no significant time delay).

This correlation could be explained by an effect of ERK on tissue mechanics [30–32] or an effect of tissue deformation or density on ERK [31, 33–36]. To test those hypotheses, we induced local mechanical perturbations using two laser perturbation approaches. Local laser wounding of the notum induces cell

ERK activity on the left and low ERK activity for the right). Blue arrows: ectopic nuclear accumulation. White dashed lines: clone boundaries. Scale bars represent 10 μm.

(D) Western blot of dpERK (top) and total ERK (bottom) in S2 cells upon inhibition of ERK phosphorylation by trametinib (10 μM; a potent inhibitor of MEK, left scheme) at different time after drug treatment (in minutes). Control band: DMSO treatment (30 min after adding DMSO). Similar results were obtained at 1 μM.

(E) Live imaging of larval haemocytes primary culture expressing tub-miniCic upon treatment with 10 μM trametinib (top) or DMSO (bottom). Time (minutes) after drug deposition is shown. Dotted circles: nuclei (detected by transmitted light). Scale bars represent 10 μm. (Right graph) Mean normalized miniCic nuclear intensity after drug treatment (two independent experiments) is shown. Error bars are SEM.

(F) Snapshots of a live pupal notum expressing endo-Ecad::GFP and miniCic (local z-projection) at different time after pupal formation (APF). Anterior: left; posterior: right; midline in the center (see left scheme). Scale bar represents 20 μm. Right heatmap: averaged miniCic signal over the full movie is shown; cell death events over the full movie are shown (bottom right picture; one dot = one elimination).

See also Figure S3 and Video S2.

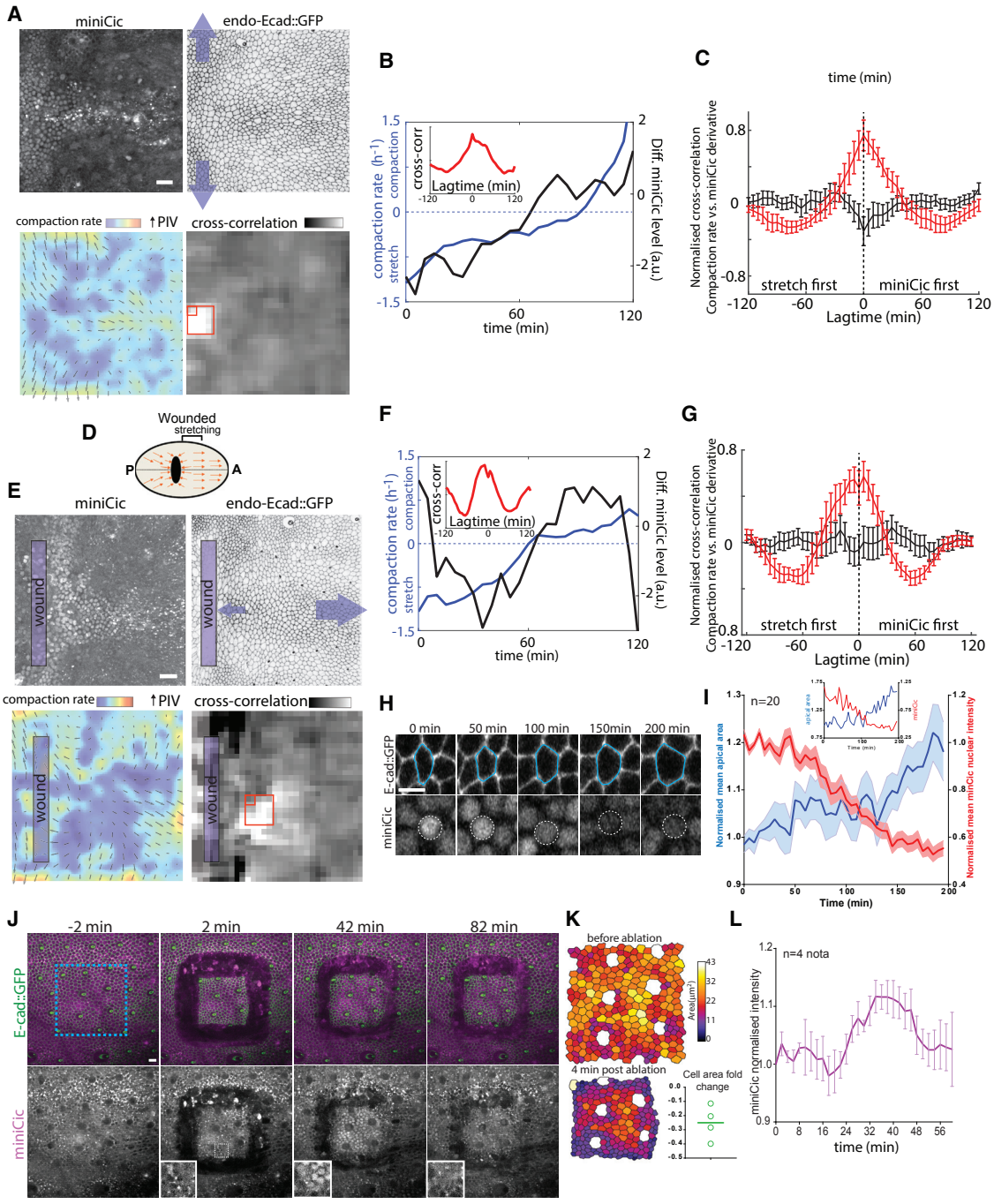

Figure 5. Tissue Stretching or Compaction Can Increase or Decrease ERK Activity Ectopically

(A, D, and E) Pupal notum expressing endo-Ecad::GFP and miniCic::mCherry during a spontaneous phase of tissue stretching orthogonal to the antero-posterior axis (A; blue arrows) or during stretching induced by laser wounding (E) schematic of the experiment in (D); orange arrows show tissue displacement; A, anterior right; P, Posterior left. From left to right and top to bottom: (1) miniCic::mCherry fluorescent signal; (2) inverted endo-Ecad::GFP; (3) overlay of compaction rate and PIV images averaged over 50 min (PIV biggest arrow: 5 μm/hr in A and 10 μm/hr in E; compaction rate scale bar −0.35 to 0.7 hr^{-1}; blue, stretching; red, compaction); and (4) pseudo-image of the local cross-correlation value between compaction rate and miniCic signal derivative for a lag time of 0 min. The peak of correlation appears in the posterior central region (white region) in (A) and anterior to the wound in (E). Scale bars represent 20 μm.

(B and F) Representative plots of the compaction rate (blue) and miniCic intensity derivative (black) in a single PIV square (small red rectangles, A and E) during the spontaneous stretch (B) and during wounding (F). Insets, normalized cross-correlation of compaction rate versus the derivative of miniCic for those curves is shown.

(C and G) Mean normalized cross-correlation of compaction rate versus miniCic derivative during spontaneous stretching (C) or after wounding (G; red curves) from red square regions in (A) and (E) and control areas (in black) for several nota (n = 3) and subregions. Error bars indicate SEM.

(legend continued on next page)

stretching and reduction of cell elimination anterior to the wound because of the opposite movements of the global tissue drift (anterior side) and the wound closure [9] (Figure 5D). Ectopic stretching of the tissue induced by laser wounding was sufficient to transiently upregulate ERK signaling anterior to the wound (Figure 5E, main stretch along AP axis; Video S3). Using PIV, we also observed a significant correlation between zones of stretching and upregulation of ERK activity (Figures 5F and 5G), especially anterior to the wound (bottom right, Figure 5E). This was confirmed by the significant increase of the cell apical area and the concomitant decrease of miniCic nuclear intensity at the single-cell level in the region anterior to the wound (Figures 5H and 5I). The modulation of ERK cannot be driven solely by diffusive factors from the wound, as the upregulation of ERK and the correlation were restricted to the anterior side of the wound, where stretching is stronger (Figures 5D and 5E, bottom right; Video S3). Altogether, we conclude that tissue and/or cell stretching can ectopically upregulate ERK activity.

Conversely, we then tested whether ectopic tissue compaction and/or relaxation could downregulate ERK activity. The pupal notum is globally stretched and laser severing of a piece of epithelium leads to a rapid relaxation and reduction of the isolated cells apical area [37]. Using a pulsed UV laser, we isolated a 110 × 110 μm tissue square (~300 cells), which rapidly relaxed (Figures 5J and 5K; Video S3). Tissue relaxation and/or densification was followed by a transient nuclear accumulation of miniCic peaking ~30 min after sectioning (Figures 5J and 5L; Video S3). Thus, stress release and/or tissue densification can transiently downregulate ERK activity. In this study, we used two sets of laser perturbation experiments (line wound, Figures 5E–5I; square severing, Figures 5J–5L) that led to opposite effects on ERK activity (activation or inhibition, respectively) and opposite tissue deformations (stretching or compaction). This excludes again that ERK variations were driven by diffusive factors from the laser-induced wounds. Finally, induction of tissue crowding and folding by the expression of a constitutively active form of Yorkie (*UAS-Yki^{S111A,S168A,S250A}* [38], a strong regulator of growth and survival) [39, 40] was sufficient to downregulate ERK everywhere in the notum (Figure S4). Altogether, this shows that tissue stretching or compaction can transiently upregulate or downregulate ERK activity in the pupal notum.

Compaction-Driven ERK Downregulation Is Required for Cell Elimination Near Ras^{V12} Clones and Accelerates Clone Expansion

We next tested whether ERK activity was modulated in compacted zones in between *Ras^{V12}* clones. Induction of ectopic tissue compaction through growth upregulation in *Ras^{V12}* clones led to a progressive downregulation of ERK signaling in the neighboring WT cells (Figure 6A; Video S4; region where we normally do not observe ERK downregulation; Figure 3F). The pattern of ERK inhibition correlated with the zones of high compaction rate measured by PIV (Figure 6B; $R^2 = 0.41$). Moreover, we observed a clear enrichment of apoptotic cells in zones of low ERK activity in WT cells surrounded by Ras clones (Figure S5A). We thus concluded that ERK is downregulated in compacted cells in between Ras^{V12} clones.

Next, we tested whether ERK downregulation was necessary for neighboring cell elimination. Overexpression of a secreted form of Spitz (sSptiz; *Drosophila* EGF) by *Ras^{V12}* clones could activate ERK in the neighboring cells without impacting ERK activation in *Ras^{V12}* clones (Figure S5B). This was sufficient to prevent neighboring cell elimination (Figures 6C and 6D; Video S4). It also slowed down the shrinkage of the area covered by WT cells (Figure 6E) and the expansion of the apical area of *Ras^{V12}* cells close to the clone boundaries (Figure 6F; 79% increase over 700 min for *Ras^{V12}* cells; 24% for *Ras^{V12}*, *sSpitz* cells), which are the cells that should compensate for most of the area left by the WT dying cells [41]. This suggests that cell elimination through ERK downregulation contributes to clone expansion and global replacement of the WT cells.

Finally, we wanted to make sure that WT cell elimination was indeed driven by mechanical cues rather than diffusive factors from the clones. Increasing contractility in *Ras^{V12}* cells through the overexpression of an active form of MyoII (*UAS-sqhE20E21*) [42] was sufficient to prevent *Ras^{V12}* cell expansion (Figure 6F; average cell area decrease of 18%) and strongly downregulated WT cell elimination (Figures 6C–6E; Video S4), suggesting that *Ras^{V12}* cell expansion is indeed necessary for WT cell elimination. WT cell elimination could also be driven by the secretion of Argos from *Ras^{V12}* clones and the consequent sequestration of Spitz/EGF [43]. However, preventing Argos accumulation in *Ras^{V12}* clones by dsRNA did not abolish WT cell elimination near active Ras clones (Figures S5C–S5E; Video S4). Those experiments confirmed that cell elimination was driven by mechanical cues rather than purely diffusive factors from the Ras clones.

Altogether, we conclude that tissue compaction and/or a reduction of cell tension can rapidly downregulate ERK activity *in vivo*, which triggers cell elimination through the upregulation of Hid. This modulation of ERK is responsible for cell elimination near *Ras^{V12}* clones, which contributes significantly to clone expansion and may eventually lead to replacement of the entire WT cell population.

DISCUSSION

EGFR/ERK/Hid pathway has been previously involved in tissue homeostasis and cell number regulation [44, 45]. For instance,

(H) Snapshots of a cell in the stretched region anterior to the wound. Cell contour in blue shows corresponding nucleus with miniCic signal with white dotted circles. Scale bar represents 10 μm.

(I) Averaged normalized cell apical area and miniCic nuclear signal in the stretched region (n = 20 cells). Light colors: SEM. Inset: single curve for the cell shown in (H) is shown.

(J) Local projection of a live pupal notum expressing endo-Ecad::GFP (green) and miniCic::mCherry (magenta, bottom) at different times after laser sectioning of a square (blue) of 110 × 110 μm. Insets: miniCic signal from representative nuclei of the isolated piece of tissue is shown. Scale bar represents 10 μm.

(K) Segmentation of the isolated tissue prior and post-sectioning (apical area in pseudo-colors). Bottom right graph: average variation of cell apical area is shown (one dot per notum; [A final − A initial]/A initial).

(L) Averaged normalized miniCic intensity in the isolated tissue square (t0 = sectioning; 4 nota). Error bars indicate SEM.

See also Figure S4 and Video S3.

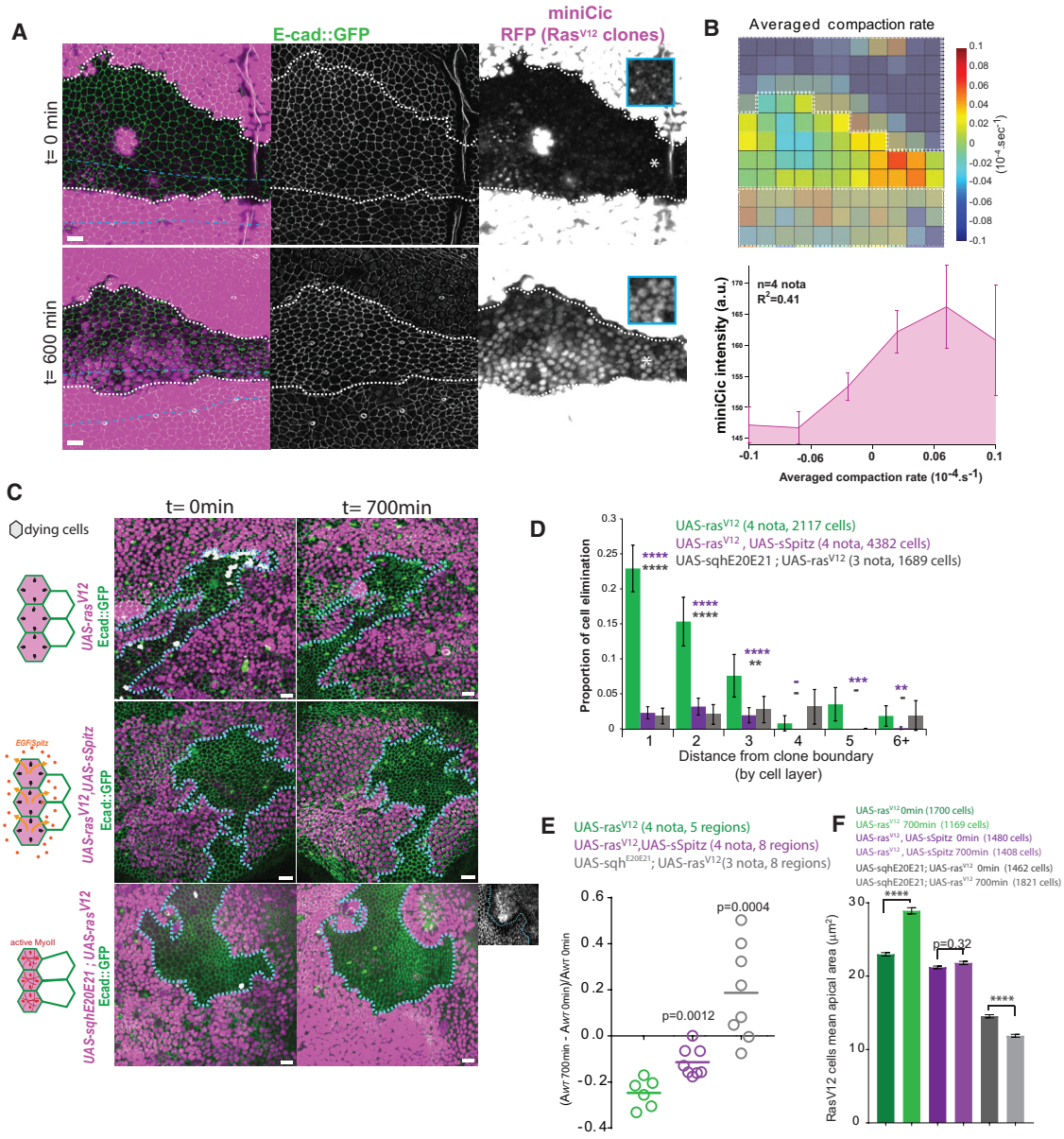

Figure 6. Mechanical Competition Eliminates Cells through Compaction-Driven ERK Downregulation

(A) Snapshots (0 and 600 min; local z-projections) of a live pupal notum; endo-Ecad::GFP (green) miniCic (magenta); induction of *Ras^{V12}* in clones (RFP, strong magenta, white dashed lines); midline: blue dotted lines; blue rectangles: single plane miniCic signal from asterisk regions. Scale bars represent 10 μm.

(B) Top: map of the averaged compaction rate (PIV, white dashed lines: clone boundaries). Red: compaction; blue: stretching. Bottom: averaged local miniCic intensity at 600 min for a given local compaction rate is shown (4 nota). R^2: Pearson correlation coefficient. Error bars indicate SEM.

(C) z-projections (0 min and after 700 min) of live pupal nota expressing endo-Ecad::GFP (green) upon conditional induction of *Ras^{V12}*, *Ras^{V12}* and *sSpitz* (*Drosophila* EGF), or *Ras^{V12}* and *sqhE20E21* (constitutively active Myosin II regulatory light chain) in clones (RFP, magenta, blue dashed lines: contours). Dying cells are shown in white. Left schemes: expected deformations of the cells are shown (clone, purple). Bottom right inset: E-cad::GFP in Ras and active MyoII clones are shown. Scale bars represent 10 μm.

(D) Probability of cell death for a given distance to clone boundaries (in cell rows). ****$p < 10^{-4}$; ***$p < 10^{-3}$; **$p < 10^{-2}$; -$p > 0.05$; Fisher exact test with *UAS-ras^{V12}* (green bars). Error bars indicate 95% confidence interval.

(E) Evolution of the area covered by WT cells (one circle = one region surrounded by several clones). Bars indicate averages; t test with *UAS-ras^{V12}* (green).

(F) Average *ras^{V12}* cell apical area (three first cells layers of the clones) at 0 and 700 min. Mann-Whitney tests between time points; ****$p < 10^{-4}$ from 4, 4, and 3 nota. Error bars indicate SEM. Upon activation of MyoII, cells are already smaller at t0 because transcription was activated 8 hr before.

See also Figure S5 and Video S4.

modulation of segment size in *Drosophila* embryo can be adjusted by cell death regulated by EGFR/Hid and the limited source of Spitz/EGF [45, 46]. A similar mechanism is involved in the regulation of the number of interommatidial cells in the fly retina [19, 47–50] or the number of glia cells in the embryo [51]. Those studies are based on the modulation of EGFR/ERK and death triggered by limiting extracellular ligands. Here, we show that ERK activity can also be modified by tissue mechanics *in vivo*, which changes the probability of cell survival. Modulation of ERK activity by mechanical stress and/or tissue density has been previously described in cell culture [31, 33, 34, 36, 52] and *in vivo* [35]. Here, we provide the first evidence of a mechanical modulation of ERK playing an instructive role for cell survival and death during competitive interactions between two cell types *in vivo*. So far, most of the studies of mechanotransduction *in vivo* focused on the regulation of Hippo/Yap-Taz pathway [11], whose transcriptional outputs should act on hours timescale. Our results suggest that ERK modulation could act on cell survival in a few tens of minutes (see Figure 4) through the phosphorylation [18] and/or transcriptional regulation [19] of Hid.

Interestingly, global EGFR depletion increased the rate of cell elimination everywhere in the notum (Figures 2B–2D), irrespective of the deformation status of the cells. Accordingly, we found that cells are not any more sensitive to stretching upon EGFR depletion (Figures S6A–S6C; Video S5). This suggests that a ubiquitous basal activity of EGFR is required for cell survival everywhere in the notum, which could be then modulated by tissue deformation. We found that tissue stress and/or compaction can modulate ERK activity and that part of the ERK dynamics correlated with tissue deformations. However, it is very likely that the complex spatiotemporal pattern of ERK activity in the pupal notum (e.g., global downregulation 16 or 17 hr APF and global upregulation 20 hr APF; Video S2) is also controlled by currently unknown patterning genes. EGFR/ERK modulation by deformation may be required to fine tune its activity, to coordinate in time and space cell elimination, and to regulate the number of cells that will be eliminated. A high rate of cell elimination could lead to higher cell spacing and/or an increase of tissue tension, which would feedback negatively on cell elimination through ERK activation. Moreover, the mutual regulation of ERK and mechanics [30–32] could generate complex temporal dynamics and self-organized properties [31].

Although we do not know which molecular effectors of ERK pathway are sensitive to mechanical stress, epistasis experiments suggest that modulation occurs upstream and/or at the level of EGFR (see Figures S6A–S6C; Video S5). Accordingly, a large pool of EGFR is located at adherens junctions (Figure S6D) compatible with a modulation of EGFR activity by apical cell geometry and/or mechanical stress. So far, we did not observe obvious variations of the location and concentration of EGFR in the midline compared to the rest of the notum (Figure S6D), arguing for a mechanism based on a modulation of EGFR activity rather than a direct modulation of its concentration/localization.

The correlation between tissue stretching or compaction and ERK activity could be explained by different parameters, including membrane tension, cell apical surface, and/or changes in cell volume. The transient ERK downregulation observed after tissue severing and the correlation between compaction rate and ERK activity suggest that ERK is sensitive to strain rate rather than absolute cell size and/or tissue density. Similarly, compressive forces rather than absolute tissue density are responsible for spontaneous MDCK cell elimination [6]. Further exploration of the single cell parameters correlating with ERK fluctuations will help to identify the relevant factors modulating ERK.

Although our data support a central role for ERK in modulating cell survival in the pupal notum, we cannot predict fully accurately which cell will engage in apoptosis based on miniCic signal. For instance, we do not know whether caspase activation is triggered by the temporal dynamics or ERK or/and by its absolute levels. Moreover, the probability of cell elimination is still higher in the midline compared to the rest of the tissue upon EGFR depletion (Figures 2C and 2D, 0.75 and 0.42, respectively, versus 0.29 and 0.03 for control clones; Figures 1C and 1D), suggesting that other currently unknown factors also modulate the susceptibility to cell death in the midline. This is in agreement with the absence of ERK downregulation preceding caspase activation in 25% of the midline dying cells (Figure 4). Further work will be required to identify all the factors modulating cell survival in the notum.

Finally, the contribution of compaction-induced ERK inhibition to cell elimination and Ras^{V12} clone expansion may be relevant for other competition scenarios and in pathological conditions. Yki activation in clones was also shown to trigger WT cell deformation and their death in the pupal notum [41]. Cells mutant for the apico-basal polarity protein Scribble are also eliminated through the downregulation of EGFR/ERK [53], although this is driven in that case by the ligand Sas and the tyrosine phosphatase PTP10D. Finally, compaction-driven ERK downregulation could be relevant for the elimination of misspecified cells in *Drosophila* wing imaginal disc, which has been associated with an increase of contractility at the clone boundary, leading to cell compaction within the clone [54]. Constitutively active mutant forms of Ras are present in one third of human cancers [55]. Our study suggests that blocking mechanical-induced cell elimination by ERK activation can significantly slow down the expansion of tumoral cells. This opposite role of ERK in tumors (promotion of tumoral cell growth and survival) and the surrounding cells (resistance to mechanical stress) may explain the limited success of Ras/Raf/ERK-targeted cancer therapies [55].

STAR★METHODS

Detailed methods are provided in the online version of this paper and include the following:

- KEY RESOURCES TABLE
- CONTACT FOR REAGENT AND RESOURCE SHARING
- EXPERIMENTAL MODEL AND SUBJECT DETAILS
  - *Drosophila melanogaster* husbandry
  - *Drosophila melanogaster* strains
  - Genotypes of the experimental model
  - S2R+ cells
- METHOD DETAILS
  - Replication, sample size and strategy for randomization
  - Immunostaining
  - Design of the miniCic sensor
  - Western blot

- Analysis of adult thorax defects
- Imaging of haemocytes and drug treatment
- Notum live imaging, image processing and cell death analysis
- Adaptive local z-projection and analysis of miniCic::mCherry
- Nuclear miniCic quantification and Scat3 imaging
- Particle Image Velocimetry, cross-correlation and tissue wounding

- QUANTIFICATION AND STATISTICAL ANALYSIS
- DATA AND SOFTWARE AVAILABILITY

SUPPLEMENTAL INFORMATION

Supplemental Information includes six figures, one Methods file, and five videos and can be found with this article online at https://doi.org/10.1016/j.cub.2018.11.007.

ACKNOWLEDGMENTS

We thank members of R.L. lab and F. Schweisguth for critical reading of the manuscript. We are also grateful to F. Janody, M. Miura, C. Bökel, H.D. Ryoo, G. Jiménez, the Bloomington Drosophila Stock Center, the Drosophila Genetic Resource Center, the Vienna Drosophila Resource Center, and the Developmental Studies Hybridoma Bank for sharing stocks and reagents. We also thank B. Aigouy for the Packing Analyzer software and J. Ellenberg group for MyPic autofocus macro. L.V. is supported by a post-doctoral grant "Aide au Retour en France" from the FRM (Fondation pour la Recherche Médicale) (ARF20170938651); work in R.L. lab is supported by the Institut Pasteur (G5 starting package) and the ERC starting grant CoSpaDD (Competition for Space in Development and Disease) (grant number 758457). Work in E.M. lab is supported by the European Research Council, The Swiss National Foundation, and the Champalimaud Foundation.

AUTHOR CONTRIBUTIONS

E.M. and R.L. initiated the project. L.V. performed the wounding experiments, the cross-correlation analysis, the miniCic and caspase correlation, and the local projection algorithm. F.L. performed the dpERK western blot. R.L. wrote the manuscript and performed all the other experiments and analysis. Every author has commented and edited the manuscript.

DECLARATION OF INTERESTS

The authors declare no competing interests.

Received: July 25, 2018
Revised: October 1, 2018
Accepted: November 1, 2018
Published: December 13, 2018

REFERENCES

1. Merino, M.M., Levayer, R., and Moreno, E. (2016). Survival of the fittest: essential roles of cell competition in development, aging, and cancer. Trends Cell Biol. *26*, 776–788.
2. Petridou, N.I., Spiró, Z., and Heisenberg, C.P. (2017). Multiscale force sensing in development. Nat. Cell Biol. *19*, 581–588.
3. Guillot, C., and Lecuit, T. (2013). Mechanics of epithelial tissue homeostasis and morphogenesis. Science *340*, 1185–1189.
4. Irvine, K.D., and Shraiman, B.I. (2017). Mechanical control of growth: ideas, facts and challenges. Development *144*, 4238–4248.
5. Eisenhoffer, G.T., Loftus, P.D., Yoshigi, M., Otsuna, H., Chien, C.B., Morcos, P.A., and Rosenblatt, J. (2012). Crowding induces live cell extrusion to maintain homeostatic cell numbers in epithelia. Nature *484*, 546–549.
6. Saw, T.B., Doostmohammadi, A., Nier, V., Kocgozlu, L., Thampi, S., Toyama, Y., Marcq, P., Lim, C.T., Yeomans, J.M., and Ladoux, B. (2017). Topological defects in epithelia govern cell death and extrusion. Nature *544*, 212–216.
7. Wagstaff, L., Goschorska, M., Kozyrska, K., Duclos, G., Kucinski, I., Chessel, A., Hampton-O'Neil, L., Bradshaw, C.R., Allen, G.E., Rawlins, E.L., et al. (2016). Mechanical cell competition kills cells via induction of lethal p53 levels. Nat. Commun. *7*, 11373.
8. Marinari, E., Mehonic, A., Curran, S., Gale, J., Duke, T., and Baum, B. (2012). Live-cell delamination counterbalances epithelial growth to limit tissue overcrowding. Nature *484*, 542–545.
9. Levayer, R., Dupont, C., and Moreno, E. (2016). Tissue crowding induces caspase-dependent competition for space. Curr. Biol. *26*, 670–677.
10. Pereira, A.M., Tudor, C., Kanger, J.S., Subramaniam, V., and Martin-Blanco, E. (2011). Integrin-dependent activation of the JNK signaling pathway by mechanical stress. PLoS ONE *6*, e26182.
11. Panciera, T., Azzolin, L., Cordenonsi, M., and Piccolo, S. (2017). Mechanobiology of YAP and TAZ in physiology and disease. Nat. Rev. Mol. Cell Biol. *18*, 758–770.
12. Norman, M., Wisniewska, K.A., Lawrenson, K., Garcia-Miranda, P., Tada, M., Kajita, M., Mano, H., Ishikawa, S., Ikegawa, M., Shimada, T., and Fujita, Y. (2012). Loss of Scribble causes cell competition in mammalian cells. J. Cell Sci. *125*, 59–66.
13. Vincent, J.P., Fletcher, A.G., and Baena-Lopez, L.A. (2013). Mechanisms and mechanics of cell competition in epithelia. Nat. Rev. Mol. Cell Biol. *14*, 581–591.
14. Brás-Pereira, C., and Moreno, E. (2018). Mechanical cell competition. Curr. Opin. Cell Biol. *51*, 15–21.
15. Guirao, B., Rigaud, S.U., Bosveld, F., Bailles, A., López-Gay, J., Ishihara, S., Sugimura, K., Graner, F., and Bellaïche, Y. (2015). Unified quantitative characterization of epithelial tissue development. eLife *4*, e08519.
16. Jiang, C., Baehrecke, E.H., and Thummel, C.S. (1997). Steroid regulated programmed cell death during Drosophila metamorphosis. Development *124*, 4673–4683.
17. Brennecke, J., Hipfner, D.R., Stark, A., Russell, R.B., and Cohen, S.M. (2003). bantam encodes a developmentally regulated microRNA that controls cell proliferation and regulates the proapoptotic gene hid in Drosophila. Cell *113*, 25–36.
18. Bergmann, A., Agapite, J., McCall, K., and Steller, H. (1998). The Drosophila gene hid is a direct molecular target of Ras-dependent survival signaling. Cell *95*, 331–341.
19. Kurada, P., and White, K. (1998). Ras promotes cell survival in Drosophila by downregulating hid expression. Cell *95*, 319–329.
20. Astigarraga, S., Grossman, R., Díaz-Delfín, J., Caelles, C., Paroush, Z., and Jiménez, G. (2007). A MAPK docking site is critical for downregulation of Capicua by Torso and EGFR RTK signaling. EMBO J. *26*, 668–677.
21. Parsons, J.T. (2003). Focal adhesion kinase: the first ten years. J. Cell Sci. *116*, 1409–1416.
22. Kim, L.C., Song, L., and Haura, E.B. (2009). Src kinases as therapeutic targets for cancer. Nat. Rev. Clin. Oncol. *6*, 587–595.
23. Shilo, B.Z. (2014). The regulation and functions of MAPK pathways in Drosophila. Methods *68*, 151–159.
24. Inaki, M., Vishnu, S., Cliffe, A., and Rørth, P. (2012). Effective guidance of collective migration based on differences in cell states. Proc. Natl. Acad. Sci. USA *109*, 2027–2032.
25. Prober, D.A., and Edgar, B.A. (2002). Interactions between Ras1, dMyc, and dPI3K signaling in the developing Drosophila wing. Genes Dev. *16*, 2286–2299.
26. Kumar, J.P., Hsiung, F., Powers, M.A., and Moses, K. (2003). Nuclear translocation of activated MAP kinase is developmentally regulated in the developing Drosophila eye. Development *130*, 3703–3714.

27. Slack, C., Alic, N., Foley, A., Cabecinha, M., Hoddinott, M.P., and Partridge, L. (2015). The Ras-Erk-ETS-signaling pathway is a drug target for longevity. Cell *162*, 72–83.
28. Lim, B., Dsilva, C.J., Levario, T.J., Lu, H., Schüpbach, T., Kevrekidis, I.G., and Shvartsman, S.Y. (2015). Dynamics of inductive ERK signaling in the Drosophila embryo. Curr. Biol. *25*, 1784–1790.
29. Takemoto, K., Nagai, T., Miyawaki, A., and Miura, M. (2003). Spatio-temporal activation of caspase revealed by indicator that is insensitive to environmental effects. J. Cell Biol. *160*, 235–243.
30. Tanimura, S., and Takeda, K. (2017). ERK signalling as a regulator of cell motility. J. Biochem. *162*, 145–154.
31. Aoki, K., Kondo, Y., Naoki, H., Hiratsuka, T., Itoh, R.E., and Matsuda, M. (2017). Propagating wave of ERK activation orients collective cell migration. Dev. Cell *43*, 305–317.e5.
32. Ogura, Y., Wen, F.L., Sami, M.M., Shibata, T., and Hayashi, S. (2018). A switch-like activation relay of EGFR-ERK signaling regulates a wave of cellular contractility for epithelial invagination. Dev. Cell *46*, 162–172.e5.
33. Aoki, K., Kumagai, Y., Sakurai, A., Komatsu, N., Fujita, Y., Shionyu, C., and Matsuda, M. (2013). Stochastic ERK activation induced by noise and cell-to-cell propagation regulates cell density-dependent proliferation. Mol. Cell *52*, 529–540.
34. Kawabata, N., and Matsuda, M. (2016). Cell density-dependent increase in tyrosine-monophosphorylated ERK2 in MDCK cells expressing active Ras or Raf. PLoS ONE *11*, e0167940.
35. Sano, T., Kobayashi, T., Negoro, H., Sengiku, A., Hiratsuka, T., Kamioka, Y., Liou, L.S., Ogawa, O., and Matsuda, M. (2016). Intravital imaging of mouse urothelium reveals activation of extracellular signal-regulated kinase by stretch-induced intravesical release of ATP. Physiol. Rep. *4*, e13033.
36. Hirata, H., Gupta, M., Vedula, S.R., Lim, C.T., Ladoux, B., and Sokabe, M. (2015). Actomyosin bundles serve as a tension sensor and a platform for ERK activation. EMBO Rep. *16*, 250–257.
37. Bonnet, I., Marcq, P., Bosveld, F., Fetler, L., Bellaïche, Y., and Graner, F. (2012). Mechanical state, material properties and continuous description of an epithelial tissue. J. R. Soc. Interface *9*, 2614–2623.
38. Oh, H., and Irvine, K.D. (2009). In vivo analysis of Yorkie phosphorylation sites. Oncogene *28*, 1916–1927.
39. Thompson, B.J., and Cohen, S.M. (2006). The Hippo pathway regulates the bantam microRNA to control cell proliferation and apoptosis in Drosophila. Cell *126*, 767–774.
40. Huang, J., Wu, S., Barrera, J., Matthews, K., and Pan, D. (2005). The Hippo signaling pathway coordinately regulates cell proliferation and apoptosis by inactivating Yorkie, the Drosophila Homolog of YAP. Cell *122*, 421–434.
41. Tsuboi, A., Ohsawa, S., Umetsu, D., Sando, Y., Kuranaga, E., Igaki, T., and Fujimoto, K. (2018). Competition for space is controlled by apoptosis-induced change of local epithelial topology. Curr. Biol. *28*, 2115–2128.e5.
42. Jordan, P., and Karess, R. (1997). Myosin light chain-activating phosphorylation sites are required for oogenesis in Drosophila. J. Cell Biol. *139*, 1805–1819.
43. Klein, D.E., Nappi, V.M., Reeves, G.T., Shvartsman, S.Y., and Lemmon, M.A. (2004). Argos inhibits epidermal growth factor receptor signalling by ligand sequestration. Nature *430*, 1040–1044.
44. Liang, J., Balachandra, S., Ngo, S., and O'Brien, L.E. (2017). Feedback regulation of steady-state epithelial turnover and organ size. Nature *548*, 588–591.
45. Parker, J. (2006). Control of compartment size by an EGF ligand from neighboring cells. Curr. Biol. *16*, 2058–2065.
46. Crossman, S.H., Streichan, S.J., and Vincent, J.P. (2018). EGFR signaling coordinates patterning with cell survival during Drosophila epidermal development. PLoS Biol *16*, https://doi.org/10.1371/journal.pbio.3000027.
47. Baker, N.E., and Yu, S.Y. (2001). The EGF receptor defines domains of cell cycle progression and survival to regulate cell number in the developing Drosophila eye. Cell *104*, 699–708.
48. Yang, L., and Baker, N.E. (2003). Cell cycle withdrawal, progression, and cell survival regulation by EGFR and its effectors in the differentiating Drosophila eye. Dev. Cell *4*, 359–369.
49. Yu, S.Y., Yoo, S.J., Yang, L., Zapata, C., Srinivasan, A., Hay, B.A., and Baker, N.E. (2002). A pathway of signals regulating effector and initiator caspases in the developing Drosophila eye. Development *129*, 3269–3278.
50. Miller, D.T., and Cagan, R.L. (1998). Local induction of patterning and programmed cell death in the developing Drosophila retina. Development *125*, 2327–2335.
51. Bergmann, A., Tugentman, M., Shilo, B.Z., and Steller, H. (2002). Regulation of cell number by MAPK-dependent control of apoptosis: a mechanism for trophic survival signaling. Dev. Cell *2*, 159–170.
52. Tschumperlin, D.J., Dai, G., Maly, I.V., Kikuchi, T., Laiho, L.H., McVittie, A.K., Haley, K.J., Lilly, C.M., So, P.T., Lauffenburger, D.A., et al. (2004). Mechanotransduction through growth-factor shedding into the extracellular space. Nature *429*, 83–86.
53. Yamamoto, M., Ohsawa, S., Kunimasa, K., and Igaki, T. (2017). The ligand Sas and its receptor PTP10D drive tumour-suppressive cell competition. Nature *542*, 246–250.
54. Bielmeier, C., Alt, S., Weichselberger, V., La Fortezza, M., Harz, H., Jülicher, F., Salbreux, G., and Classen, A.K. (2016). Interface contractility between differently fated cells drives cell elimination and cyst formation. Curr. Biol. *26*, 563–574.
55. Samatar, A.A., and Poulikakos, P.I. (2014). Targeting RAS-ERK signalling in cancer: promises and challenges. Nat. Rev. Drug Discov. *13*, 928–942.
56. Karim, F.D., and Rubin, G.M. (1998). Ectopic expression of activated Ras1 induces hyperplastic growth and increased cell death in Drosophila imaginal tissues. Development *125*, 1–9.
57. Herranz, H., Hong, X., and Cohen, S.M. (2012). Mutual repression by bantam miRNA and Capicua links the EGFR/MAPK and Hippo pathways in growth control. Curr. Biol. *22*, 651–657.
58. Michel, M., Raabe, I., Kupinski, A.P., Pérez-Palencia, R., and Bökel, C. (2011). Local BMP receptor activation at adherens junctions in the Drosophila germline stem cell niche. Nat. Commun. *2*, 415.
59. Levayer, R., Hauert, B., and Moreno, E. (2015). Cell mixing induced by myc is required for competitive tissue invasion and destruction. Nature *524*, 476–480.
60. Bertet, C., Rauzi, M., and Lecuit, T. (2009). Repression of Wasp by JAK/STAT signalling inhibits medial actomyosin network assembly and apical cell constriction in intercalating epithelial cells. Development *136*, 4199–4212.
61. Valon, L., Marín-Llauradó, A., Wyatt, T., Charras, G., and Trepat, X. (2017). Optogenetic control of cellular forces and mechanotransduction. Nat. Commun. *8*, 14396.
62. Aigouy, B., Farhadifar, R., Staple, D.B., Sagner, A., Röper, J.C., Jülicher, F., and Eaton, S. (2010). Cell flow reorients the axis of planar polarity in the wing epithelium of Drosophila. Cell *142*, 773–786.
63. Jauffred, B., and Bellaiche, Y. (2012). Analyzing frizzled signaling using fixed and live imaging of the asymmetric cell division of the Drosophila sensory organ precursor cell. Methods Mol. Biol. *839*, 19–25.

STAR★METHODS

KEY RESOURCES TABLE

REAGENT or RESOURCE	SOURCE	IDENTIFIER
Antibodies		
rat anti E-cad	DSHB	DCAD2 concentrate; RRID:AB_528120
guinea pig anti Hid	gift of Don Hyong Ryu	N/A
mouse anti EcR	DSHB	Ag10.2 concentrate; RRID:AB_528208
rabbit anti dpERK	Cell Signaling	Phospho-p44/42 MAPK #4370; RRID:AB_2315112
chicken anti GFP	abCam	#13970; RRID:AB_300798
chicken anti mCherry	abCam	#205402; RRID:AB_2722769
rabbit anti-cleaved Dcp-1	Cell Signaling	#9578; RRID:AB_2721060
mouse anti-Argos	DSHB	Argos 85/2/16 concentrate; RRID:AB_528088
monoclonal mouse anti EGFR	Sigma	E29006 clone C-273; RRID:AB_609900
rabbit anti ERK	Cell Signaling	P44/42 MAPK #4695; RRID:AB_390779
Mouse anti alpha-tubulin	DSHB	12G10 concentrate; RRID:AB_1157911
Chemicals, Peptides, and Recombinant Proteins		
Trametinib	Santa Cruz	CAS 871700-17-3
Experimental Models: Cell Lines		
Drosophila S2R+ cells	François Schweisguth lab	FBrf0024118
Experimental Models: *Drosophila melanogaster* lines		
pnr-gal4 (III)	Bloomington	BDSC_3039
w ^{1118}	Bloomington	BDSC_3605
UAS-lacZ (II)	Bloomington	BDSC_8529
UAS-diap1 (III)	Bloomington	BDSC_6657
UAS-hid ds RNA (III)	VDRC	GD 8269
UAS-rpr dsRNA (II)	VDRC	KK 101234
UAS-grim dsRNA (II)	VDRC	GD 21830
hs-flp22;ubi-ECad::GFP,UAS-mRFP; act < y+ < Gal4	L. Legoff (Marseille)	N/A
UAS-ras1^{V12} (III)	From [56]	N/A
cic-Cic::GFP (Bac clone) (II)	Bloomington	BDSC_42267
UAS-egfr dsRNA (II)	VDRC	KK 107130
UAS-egfr dsRNA TRiPJF01084 (III)	Bloomington	BDSC_31526
UAS-hEC::EGFR (II)	Bloomington	BDSC_58415
endo-Ecad::GFP	Bloomington	BDSC_60584
tub-GFPBantamsensor/Cyo (II)	From [17]	N/A
UAS-dsRed Bantam sponge (III)	From [57]	N/A
ubi-Ecad::RFP (II)	From [58]	N/A
UAS-pvr dsRNA (II)	VDRC	KK 105353
UAS-fak dsRNA (III)	VDRC	GD 108608
UAS-src42A dsRNA (II)	VDRC	KK 100708
UAS-src64B dsRNA (I)	VDRC	GD 35252
UAS-pi3kCAAX (I)	Bloomington	BDSC_8294
UAS-raf^{GOF} *(III)*	Bloomington	BDSC_2033
tub-miniCic::mCherry (II)	This study	N/A
hs-flp22 ; endo-Ecad::GFP, tub-miniCic::mCherry ; act < cd2 < G4, UAS-eGFP	Bloomington and this study	BDSC_60584
endo-Ecad::GFP,tub-miniCic::mCherry	Bloomington and this study	BDSC_60584
UAS-scat3::myc (II)	From [29]	N/A

(*Continued on next page*)

Continued		
REAGENT or RESOURCE	SOURCE	IDENTIFIER
tub-miniCic::mcherry; UAS-yki $^{S111A\ S168A\ S250A}$	Bloomington combined with miniCic	BDSC_28817
hs-flp22; endo-Ecad::GFP, tub-gal80ts ; act < y+ < gal4 UAS-nlsRFP/TM6b	From [59]	N/A
hs-flp22; endo-Ecad::GFP, tub-gal80ts ; act < cd2 < gal4 UAS-eGFP/TM6b	This study	N/A
UAS-sSpitzCS, UAS-rasV12 (III)	Bloomington recombined with *UAS-ras^{V12}*	BDSC_63134
UAS-sqhE20E21 (II) ; UAS-rasV12 (III)	From [60] combined with *UAS-ras^{V12}*	N/A
UAS-argos dsRNA (II) ; UAS-rasV12 (III)	VDRC combined with *UAS-ras^{V12}*	GD 47181
Oligonucleotides		
miniCicF: ATCGCTGCGTGCGCGCTTAGGCGGCC GCAACATGCCAAAAAAGAAGAGAAAGGTATCCG CCTCCGGAGGGGGCGTGGTC	This study	N/A
miniCicR: AGAACCACCACCAGAACCACCACCGTA ATATTGAAAAACATCTGCC	This study	N/A
mCherryF: GGTGGTGGTTCTGGTGGTGGTTCTGT GTCCAAGGGCGAAGAGGAC	This study	N/A
mCherryR: GCGCGATGCCGACTGAGTAGGTCTAG ATTATTTATACAGCTCGTCCAT	This study	N/A
Recombinant DNA		
pCaSperR4-tubp-Gal80 plasmid	Addgene	#17748
Software and Algorithms		
MATLAB with Image processing toolbox and Statistics and Machine learning toolbox	Mathworks	https://fr.mathworks.com/
MatPIV	Department of Mathematics, University of Oslo	https://www.mn.uio.no/math/english/people/aca/jks/matpiv/
Fiji (ImageJ)	Fiji	https://fiji.sc/
Mypic Zen autofocus macro	Jan Ellenberg	https://git.embl.de/grp-ellenberg/mypic
Adaptive local z-projection macro (MATLAB)	This study	Supplementary information (Methods S1)
PIV algorithm (MATLAB)	[61]	N/A
Graphpad Prism8	Graphpad	https://www.graphpad.com/
Packing analyzer (now tissue miner in Fiji)	[62], Benoit Aigouy	https://idisk-srv1.mpi-cbg.de/~eaton/

CONTACT FOR REAGENT AND RESOURCE SHARING

Further information and requests for resources and reagents should be directed to and will be fulfilled by the lead contact, Romain Levayer (romain.levayer@pasteur.fr).

EXPERIMENTAL MODEL AND SUBJECT DETAILS

Drosophila melanogaster husbandry

All the experiments were performed with *Drosophila melanogaster* fly lines with regular husbandry technics. The fly food used contains agar agar (7.6 g/l), saccharose (53 g/l) dry yeast (48 g/l), maize flour (38.4 g/l), propionic acid (3.8 ml/l), Nipagin 10% (23.9 ml/l) all mixed in one liter of distilled water. Flies were raised at 25°C in plastic vials with a 12h/12h dark light cycle at 60% of moisture unless specified in the legends and in the table below (alternatively raised at 18°C or 29°C). Females and males were used without distinction for all the experiments. We did not determine the health/immune status of pupae, adults, embryos and larvae, they were not involved in previous procedures, and they were all drug and test naive.

Drosophila melanogaster strains

We used the following fly lines: *w1118* on I (Bloomington BDSC_3605), *pnr-gal4* on III (Bloomington, BDSC_3039), *UAS-lacZ* on II (Bloomington, BDSC_8529), *UAS-diap1* on III (Bloomington, BDSC_6657), *UAS-hid dsRNA* on III (VDRC, GD 8269), *UAS-rpr dsRNA* on II (VDRC, KK 101234), *UAS-grim dsRNA* on II (VDRC, GD 21830), *hs-flp22;ubi-ECad::GFP,UAS-mRFP; act < y+ < Gal4* (L. Legoff,

Marseille), *UAS-ras1^{V12}* on III (From [56]), *cic-Cic::GFP* (Bac clone) on II (Bloomington, BDSC_42267), *UAS-egfr dsRNA* on II (VDRC, KK 107130), *UAS-egfr dsRNA* on III (Bloomington, TRiPJF01084, BDSC_31526), *UAS-hEC::EGFR* on II (Bloomington, BDSC_58415), *endo-Ecad::GFP* on II (Bloomington BDSC_60584), *tub-GFPBantamsensor/Cyo* on II (from [17]), *UAS-dsRed Bantam sponge* on III (from [57]), *ubi-Ecad::RFP* on II (from [58]), *UAS-pvr dsRNA* on II (VDRC, KK 105353), *UAS-fak dsRNA* on III (VDRC, GD 108608), *UAS-src42A dsRNA* on II (VDRC, KK 100708), *UAS-src64B dsRNA* on I (VDRC, GD 35252), *UAS-pi3kCAAX* on I (Bloomington, BDSC_8294), *UAS-rafGOF* on III (Bloomington, BDSC_2033), *tub-miniCic::mCherry* on II (this study), *hs-flp22 ; endo-Ecad::GFP, tub-miniCic::mCherry ; act < cd2 < G4, UAS-eGFP* (Bloomington BDSC_60584 and this study), *endo-Ecad::GFP,tub-miniCic::mCherry* (Bloomington BDSC_60584 and this study), *UAS-scat3::myc* on II (from [29]), *tub-miniCic::mcherry; UAS-yki S111A S168A S250A* (Bloomington BDSC_28817 combined with miniCic), *hs-flp22; endo-Ecad::GFP, tub-gal80ts ; act < y+ < gal4 UAS-nlsRFP/TM6b* (from [59]), *hs-flp22; endo-Ecad::GFP, tub-gal80ts ; act < cd2 < gal4 UAS-eGFP/TM6b* (this study), *UAS-sSpitzCS, UAS-ras^{V12}* on III (Bloomington BDSC_63134 recombined with *UAS-ras^{V12}*), *UAS-sqhE20E21* (on II) *; UAS-ras^{V12}* (on III) (from [60] combined with *UAS-ras^{V12}*), *UAS-argos dsRNA* (on II) *; UAS-ras^{V12}* (on III) (VDRC GD 47181 combined with *UAS-ras^{V12}*).

Genotypes of the experimental model

We list here the fly genotypes used for each figure as well as the time of heat shock when relevant and the days after clone induction (ACI). h APF stands for hours After Pupal Formation. The number of samples (n), the stage (pupal stage, larval stage and embryos) are indicated in the table and the figure legends.

Figure	Genotype	Heat shock 37°C	Stage	n
1B	*UAS-lacZ/+ ; pnr-gal4/+*	N/A	adult	35
1B	*pnr-gal4/UAS-diap1*	N/A	adult	19
1B	*pnr-gal4/UAS-hid dsRNA*	N/A	adult	26
1B	*UAS-rpr dsRNA/+ ; pnr-gal4/+*	N/A	adult	25
1C	*hs-flp22/+; ubi-Ecad::GFP,UASmRFP/+; act < y+ < G4/+*	12 min, 3 days ACI	Pupal notum (16h APF)	4
1C	*hs-flp22/+ ; ubi-Ecad::GFP, UASmRFP/+; act < y+ < G4/UAS-hid dsRNA*	12 min, 3 days ACI	Pupal notum (16h APF)	5
1C	*hs-flp22/+ ; ubi-Ecad::GFP, UASmRFP/UAS-rpr dsRNA; act < y+ < G4/+*	12 min, 3 days ACI	Pupal notum (16h APF)	2
1E	*w ^{1118}*	N/A	Pupal notum (30h APF)	7
1F	*hs-flp22/+; endo-Ecad::GFP, tub-gal80ts/+ ; act < y+ < gal4, UAS-nlsRFP/UAS-ras^{V12}*	30 min, 1 week 18°C, 24h 29°C	Pupal notum (30h APF)	4
2A	*cic-Cic::GFP (Bac clone) (II)*	N/A	Pupal notum (30h APF)	7
2B	*UAS-lacZ/+ ; pnr-gal4/+*	N/A	adult	35
2B	*UAS-egfr dsRNA/+ ; pnr-gal4/+*	N/A	adult	23
2B	*pnr-gal4/UAS-hid dsRNA*	N/A	adult	26
2B	*UAS-egfr dsRNA/+ ; UAS-hid dsRNA/pnr-gal4*	N/A	adult	20
2C	*hs-flp22/+ ; ubi-Ecad::GFP, UASmRFP/UAS-egfr dsRNA; act < y+ < G4/+*	12 min, 3 days ACI	Pupal notum (16h APF)	3
2C	*hs-flp22/+ ; ubi-Ecad::GFP, UASmRFP/UAS-hegfr::GFP; act < y+ < G4/+*	12 min, 3 days ACI	Pupal notum (16h APF)	3
S1A	*endo-Ecad::GFP*	N/A	Pupal notum (30h APF)	3
S1B	*tub-GFPBantamsensor/ubi-Ecad::RFP*	N/A	Pupal notum (16h APF)	3
S1C	*pnr-gal4/UAS-dsRed Bantam sponge*	N/A	Pupal notum (30h APF)	4
S1D,E	*hs-flp22/+ ; ubi-Ecad::GFP, UASmRFP/+; act < y+ < G4/UAS-dsRed Bantam sponge*	12 min, 3 days ACI	Pupal notum (16h APF)	2
S1F	*w^{1118}*	N/A	Pupal notum (30h APF)	5
S2A	*UAS-pvr dsRNA/+ ; pnr-gal4/+*	N/A	adult	10
S2A	*UAS-fak dsRNA/pnr-gal4*	N/A	adult	10
S2A	*UAS-src42A dsRNA/+ ; pnr-gal4/+*	N/A	adult	13
S2A	*UAS-src64B dsRNA/+ ; ;pnr-gal4/+*	N/A	adult	13

(*Continued on next page*)

Continued

Figure	Genotype	Heat shock 37°C	Stage	n
S2B	*hs-flp22/UAS-pi3kCAAX; ubi-Ecad::GFP, UASmRFP/+; act < y+ < G4/+*	12 min, 3 days ACI	Pupal notum (16h APF)	2
S2C	*hs-flp22/+;ubi-Ecad::GFP,UASmRFP/+; act < y+ < G4/UAS-raf^{GOF}*	12 min, 2 days ACI	Pupal notum (16h APF)	2
3B	*tub-miniCic::mCherry (II)*	N/A	Wing imaginal disc and eye imaginal disc from L3 wandering stage	10
3C	*hs-flp22/+ ; endo-Ecad::GFP, tub-miniCic::mCherry/ UAS-egfr dsRNA ; act < cd2 < G4, UAS-eGFP/+*	12 min, 2 days ACI	Pupal notum (20h APF)	6
3C	*hs-flp22/+ ; endo-Ecad::GFP, tub-miniCic::mCherry/ UAS-hegfr::GFP; act < cd2 < G4, UAS-eGFP/+*	12 min, 2 days ACI	Pupal notum (20h APF)	4
3E	*tub-miniCic::mCherry (II)*	N/A	Haemocytes from L3 wandering stage larvae	2 cultures
3F	*endo-Ecad::GFP, tub-miniCic::mCherry*	N/A	Pupal notum (16h APF)	3
S3A	*tub-miniCic::mCherry*	N/A	Embryos stage 5 to 7	56
S3B	*endo-Ecad::GFP, tub-miniCic::mCherry*	N/A	Pupal notum (16h APF)	1
4A-C	*tub-miniCic::mCherry/UAS-Scat3 ; pnr-gal4/+*	N/A	Pupal notum (16h APF)	2
5A-C	*endo-Ecad::GFP, tub-miniCic::mCherry*	N/A	Pupal notum (20h APF)	3
5E-I	*endo-Ecad::GFP, tub-miniCic::mCherry*	N/A	Pupal notum (20h APF)	3
5J-L	*endo-Ecad::GFP, tub-miniCic::mCherry*	N/A	Pupal notum (30h APF)	4
S4A-C	*hs-flp22/+ ; endo-Ecad::GFP, tub-gal80ts/tub-miniCic::mCherry; act < cd2 < G4, UAS-eGFP/ UAS-yki $^{S111A\ S168A\ S250A}$*	40 min, 1 week 18°C, 24h 29°C	Pupal notum (30h APF)	10
6A,B	*hs-flp22/+; endo-Ecad::GFP, tub-gal80ts/tub-miniCic::mCherry ; act < y+ < gal4, UAS-nlsRFP/UAS-ras^{V12}*	30 min, 1 week 18°C, 24h 29°C	Pupal notum (20h APF)	4
6C-F	*hs-flp22/+; endo-Ecad::GFP, tub-gal80ts/+ ; act < y+ < gal4, UAS-nlsRFP/ UAS-ras^{V12}*	30 min, 1 week 18°C, 24h 29°C	Pupal notum (20h APF)	4
6C-F	*hs-flp22/+; endo-Ecad::GFP, tub-gal80ts/+ ; act < y+ < gal4, UAS-nlsRFP/ UAS-ras^{V12}, UAS-sSpitzCS*	30 min, 1 week 18°C, 24h 29°C	Pupal notum (20h APF)	4
6C-F	*hs-flp22/+; endo-Ecad::GFP, tub-gal80ts/UAS-sqhE20E21 ; act < y+ < gal4, UAS-nlsRFP/ UAS-ras^{V12}*	30 min, 1 week 18°C, 24h 29°C	Pupal notum (20h APF)	3
S5A	*hs-flp22/+;endo-Ecad::GFP,tub-gal80ts/ tub-miniCic::mCherry ; act < y+ < gal4, UAS-nlsRFP/UAS-ras^{V12}*	30 min, 1 week 18°C, 24h 29°C	Pupal notum (30h APF)	4
S5B	*hs-flp22/+;endo-Ecad::GFP,tub-gal80ts/ tub-miniCic::mCherry ; act < y+ < gal4, UAS-nlsRFP/UAS-ras^{V12}*	30 min, 1 week 18°C, 24h 29°C	Pupal notum (30h APF)	4
S5B	*hs-flp22/+;endo-Ecad::GFP,tub-gal80ts/ tub-miniCic::mCherry; act < y+ < gal4, UAS-nlsRFP/ UAS-ras^{V12}, UAS-sSpitzCS*	30 min, 1 week 18°C, 24h 29°C	Pupal notum (30h APF)	6
S5C	*hs-flp22/+;endo-Ecad::GFP,tub-gal80ts/+; act < y+ < gal4, UAS-nlsRFP/ UAS-ras^{V12}*	30 min, 1 week 18°C, 24h 29°C	Pupal notum (30h APF)	3
S5C	*hs-flp22/+;endo-Ecad::GFP,tub-gal80ts/UAS-argos dsRNA; act < y+ < gal4,UAS-nlsRFP/UAS-ras^{V12}*	30 min, 1 week 18°C, 24h 29°C	Pupal notum (30h APF)	3
S5D,E	*hs-flp22/+;endo-Ecad::GFP,tub-gal80ts/UAS-argos dsRNA; act < y+ < gal4,UAS-nlsRFP/UAS-ras^{V12}*	30 min, 1 week 18°C, 24h 29°C	Pupal notum (20h APF)	2
S6A-C	*hs-flp22/+ ; ubi-Ecad::GFP, UASmRFP/UAS-egfr dsRNA; act < y+ < G4/+*	12 min, 3 days ACI	Pupal notum (16h APF)	3
S6D	*endo-Ecad::GFP*	N/A	Pupal notum (25h APF)	5

S2R+ cells

S2R+ cells were cultured in Schneider's *Drosophila* medium at 25°C with 10% fetal bovine serum, penicillin and streptomycin. The line was provided by the group of François Schweisguth who originally obtained the line from the DGRC.

METHOD DETAILS

Replication, sample size and strategy for randomization

Data were not analyzed blindly. At least two independent replicates were performed for each experiment (the exact number is given in Figure legends and in the Experimental Model and Subject Details section). No specific method was used to predetermine the number of samples. We did not exclude any data/subject.

Immunostaining

Dissection and immunostainings of nota were performed as indicated in [63] with standard formaldehyde fixation and permeabilisation/washes in PBT 0.4% Triton. Briefly, the nota where pinched on a small plates containing silicone, dissected in PBS, fixed in 4% formaldehyde solution, washed in PBT 0.4% triton, stained with primary antibody solution washed and then stained with secondary antibody solution. Immunostaining of wing imaginal discs and eye imaginal discs were performed on L3 wandering stage larvae and fixed in 4% formaldehyde and permeabilised/washed in PBT. Immunostaining of embryos were performed using standard formaldehyde and heptane/methanol protocol, with permeabilisation in PBS Tween (0.05%). The following antibodies/markers were used: rat anti E-cad (DCAD2 concentrate, DSHB, 1/50), guinea pig anti Hid (1/50, strepatavidin amplified, gift of Don Hyong Ryu), mouse anti EcR (DSHB Ag10.2 concentrated, 1/100), rabbit anti dpERK (Cell signaling, #4370, 1/100), chicken anti GFP (abCam, #13970, 1/500), chicken anti mCherry (abCam, #205402, 1/200), rabbit anti-cleaved Dcp-1 (Cell Signaling, #9578, 1/50), mouse anti-Argos (DSHB concentrated, 1/50), monoclonal mouse anti EGFR (Sigma, E29006 clone C-273, 1/50). Secondary antibodies were all Invitrogen secondary antibodies produced in goat with Alexa 488,555 or 633. Dissected nota were mounted in Vectashield with DAPI (Vectorlab) and stained embryos were mounted in Aquapolymount media. They were imaged on a Leica confocal SP8 or a Zeiss lsm880 using a 63X oil immersion objective N.A. 1.3. Unless specified, images shown are maximal z-projection containing adherens junction plane.

Design of the miniCic sensor

The C-ter part of Capicua containing the C2 and C1 domains but lacking the DNA binding domain (HMG box) was PCR amplified from a cDNA clone (DGRC clone FI04109, starting at base number 2687, sequence: *TCCGCCTCCGGAGGGGGCGTGGTC*) adding a NLS site in N-ter right after the ATG. The following primers were used:

miniCicF

ATCGCTGCGTGCGCGCTTAGGCGGCCGCAACATGCCAAAAAAGAAGAGAAAGGTATCCGCCTCCGGAGGGGGCGTGGTC

miniCicR

AGAACCACCACCAGAACCACCACCGTAATATTGAAAAACATCTGCC

The reverse primer contains 23 overlapping nucleotides for the fusion with mCherry. mCherry was PCR amplified with the following primers containing the flexible linker GGGSGGGS in Nter:

mCherryF

GGTGGTGGTTCTGGTGGTGGTTCTGTGTCCAAGGGCGAAGAGGAC

mCherryR

GCGCGATGCCGACTGAGTAGGTCTAGATTATTTATACAGCTCGTCCAT

Fusion was performed by performing a PCR on the two first PCR products using the miniCicF and the mCherryR primers alone. The fusion product was inserted in pC4-tub-gal80 using the NotI and XbaI sites after removal of the Gal80 through digestion, purification and ligation. The construct was validated by sequencing and injected by Bestgene (P-element insertion).

Western blot

S2R+ cells were cultured in Schneider's *Drosophila* Medium with 10% fetal bovine serum, penicillin and streptomycin. Cells were plated at a density of $2x10^6$ cells into twelve well plates and incubated at 25°C. 24h after plating, they were treated with Trametinib 10 μM (initial stock 10mM in DMSO) or with DMSO alone (1/1000). Cellular extracts were prepared at indicated time post treatment and analyzed by immunoblotting. The following primary antibodies were used: phospho-Erk(Thr202/Tyr204) (1/1000, Cell signaling, #4370), total-Erk (1/1000, Cell signaling, #4695) and alpha-tubulin(1/5000, DSHB, 12G10 concentrated).

Analysis of adult thorax defects

Adult thorax defects were analyzed on adult female thorax raised at 25°C. For Figure 1B we measured the width of the midline divided by the averaged width of the two adjacent SOP rows along a line connecting the two aDC macrochaetaes (log2 scale). For Figure 2B we measured the width of the *pnr* domain (distance between the two aDC macrochaetaes) divided by the total width of the thorax (distance between the two pSA macrochaetae) and plotted the log2 of the ratio.

Imaging of haemocytes and drug treatment

Primary culture of haemocytes was performed by bleeding ten larvae expressing *tub-miniCic::mCherry* that were first washed in ethanol, dried on a piece of paper and resuspended in 200 μL of S2 medium on a square of parafilm. After bleeding with forceps each larvae, the 200 μL were deposed in a MaTek Petri dish (P35G-1.5-10-C) and we let the cells sediment and adhere for 30min. The media was then supplemented by 2mL of S2 medium. The dish was placed on a LSM800 point scanning confocal (63X oil N.A. 1.3) and acquisition was launched with a transmitted light channel and mCherry channel (one z stack/min). Trametinib (Santa Cruz, 10mM stock in DMSO, final concentration 10 μM) or DSMO (1/1000) were added in the medium at the onset of the movie. Nuclear miniCic signal was measured by tracking manually the nucleus using the transmission light channel on Fiji, measuring mCherry intensity and normalizing intensity by intensity at t0.

Notum live imaging, image processing and cell death analysis

Notum live imaging was performed as described previously [9]. Briefly, the pupae were collected at the white stage (0 hour after pupal formation), aged at 29°, glued on double sided tape on a slide and surrounded by two spacers composed of stacks of 4 #1 20x20mm coverslips glued with nail polisher. The pupal case was opened up to the abdomen using forceps and mounted with a 20x40mm #1.5 coverslip where we buttered halocarbon oil 10S. The coverslip was then glued on the spacers using fast drying nail polisher. Pupae were collected 48 or 72h after clone induction and dissected 16-18h after pupae formation (APF). Pupae were dissected and imaged on a confocal spinning disc microscope (Till photonics) with a 40X oil objective (N.A. 1.35) using tile imaging (6 to 12 tiled positions) or a point scanning confocal microscope Leica SP8 with a 63X objective (N.A. 1.3), or a Zeiss LSM800 or a LSM880 equipped with a fast Airyscan using an oil 40X objective (N.A. 1.3), Z stacks (1 μm/slice), every 5min using autofocus at 25°C. The autofocus was performed using E-cad::GFP plane as a reference (Tillphotonics and Leica LAS provided option) or the autofluorescence of the cuticle in far red (using a Zen Macro developed by Jan Ellenberg laboratory, MyPic). Movies were performed in the nota close to the scutellum region containing the midline and the aDC and pDC macrochaetae. Movies shown are maximum projections or adaptive local z-projection (see below for details). Total duration was always 700min (except for Figure 6A, 600min, Figures 3F, 4, and 5). For imaging of *UAS-ras^{V12}* clones, the cross and the progeny were kept at 18°C, and the pupae were switched to 29°C 8 hours prior to the movie for conditional activation (clones induced by the following lines: *hs-flp22; endo-Ecad::GFP, tub-gal80ts ; act < y+ < gal4 UAS-nlsRFP/TM6b* or *hs-flp22; endo-Ecad::GFP, tub-gal80ts ; act < cd2 < gal4 UAS-GFP*) and imaged at 29°C. The midline covers all the cells surrounded by the two most central lines of sensory organ precursors (SOP, located at the end of the movies). Every cell extrusion event was localized manually and marked using Fiji. The probability of extrusion was obtained by dividing the total number of extruding cells in the clones divided by the initial number of cells in the clones or by doing the same for each cell layer next to Ras clones. Values from the control clones (ayGal4 alone) are coming from [9] as part of the clonal experiments were performed during the same period. Note that we did the same experiment with *UAS-grim dsRNA* (GD21830) and observed a significant increase of the rate of cell death in and outside the midline (not shown here, all Grim dsRNA lines have multiple off targets). In the figures, cells were marked as dying cells if they died or if at least one of their daughter cells died before the end of the movie.

For the quantification of the area covered by WT cells during competition with Ras, regions of WT cells surrounded by at least two Ras clones were defined on Fiji and their area was measured at the onset of the movie and after 700min. Ras cell area was obtained after segmentation of the images at the onset of the movie and after 700min using packing analyzer Fiji plugin [62]. We measured apical area of the three first layers of cells near clone boundaries.

Adaptive local z-projection and analysis of miniCic::mCherry

All the image of miniCic::mCherry in the notum were obtained through a custom made adaptive local z-projection procedure wrote on MATLAB (to avoid projection of the autofluorescence signal of the cuticle and projection of more basal planes). The procedure can be found in the Supplemental information (Methods S1). For every time point, a reference channel was used (here E:cad::GFP), the image was subdivided in 40x40px (1px = 0.18 μm) square and the plane with the highest standard deviation was selected. The search window was moved in x and y 10px by 10px. The obtained z-profile was then smoothened in x and y using a Gaussian blur (2px width). miniCic signal was then obtained by calculating the median of the intensity over seven planes centered on a reference plane located 6 μm basally to the local E-cad reference plane. Note that similar results could be obtained by using maximum projection instead of the median. For every movie, we checked on the raw files that no nuclear signal of miniCic was lost because of projection errors.

Nuclear miniCic quantification and Scat3 imaging

Live pupal nota expressing UAS-Scat3 with *pnr-gal4* driver and miniCic were imaged on a LSM880 point scanning confocal (one stack every 5min or 10min). Images were pretreated with local z-projection (see above, YFP used as a reference channel, average of 7 planes around the plane of reference). Image ratios of YFP over CFP fluorescent channels were then calculated (FRET signal). Cells showing a clear caspase activation (low YFP/CFP ratio) were selected manually. The miniCic channel was also cut according to those positions and smaller stacks of 15 time frames were created (1 stack/10 min). Positions of the nuclei were selected manually over the 15 frames for all the selected cells and both YFP/CFP ratio and miniCic mean intensity values were quantified in boxes of 2 μm squares centered on those positions. The average profiles were obtained by aligning the curves on the point of maximum inflexion of the FRET signal (local minimum of the 2^{nd} derivative). Each single curve was then normalized by the values at the three first time points (70 to 50 min before caspase activation). For miniCic, the average intensity value at the three first time points was also subtracted. All the curves were then averaged. Non-ambiguous ERK downregulation (as mentioned in the text) corresponds to curves with at least a 5% increase of miniCic signal over one hour prior to caspase activation. The same procedure was performed for the control curve on randomly selected cells that do not activate caspase in same region and time developmental window as used for caspase activating cells. For those curves, alignment was made at T0 (onset of the tracking).

Particle Image Velocimetry, cross-correlation and tissue wounding

For Figure 5, we used a PIV algorithm based on the MATLAB routine described in [61]. Parameters for this PIV were analysis boxes of 64 pixels (11.5x11.5 μm ~4-5 cells), 50% overlap boxes. PIV displacements at time t were determined based on images t-5 and t+5min. Displacement maps were spatially filtered to remove noise coming from outliers.

Quantification of miniCic mCherry signal (Figures 5A–5G) are median values of mCherry signal over the analysis boxes of the PIV after performing local projection. For each notum, the region of interest (zones of maximum deformation) were subdivided in 25 squares of analysis (50% overlap). Compaction rate maps were calculated as minus the ''divergence'' function of MATLAB on the PIV vector fields. miniCic signals were smoothen over ten time frames before calculating the derivative, compaction rate were smoothen the same way. The average value was subtracted from each function to obtain variations around 0 value. Maps of cross-correlation and normalized cross-correlation between compaction rate and derivative of miniCic levels were then calculated with the ''xcorr'' MATLAB function either without or with the 'coef' option (non-normalized and normalized cross-correlation). Quantification of cross-correlations were established in stretching areas for time periods of 2 hours. Number of nota rather than number of square of analysis was used to calculate the s.e.m.. To obtain control cross-correlation curves, we computed the normalized cross-correlation of miniCic and compaction rates in regions with no obvious deformations. We also checked that there were no correlation between compaction rate of the stretched area and miniCic signals from regions outside the stretch area to make sure that the miniCic variations were specific of the zones of deformation (data not shown). Single cell tracking and segmentation (Figures 5H and 5I) was performed using packing analyzer Fiji plugin [62] and by manually tracking the corresponding miniCic nuclei for each cell. For the cross-correlation between miniCic signal and cell elimination (Figure S3D), we measured mean minCic intensity from local projections in 100x100px squares (50% overlap) and quantified the number of cell elimination occurring in those squares (disappearance of cell apical area). We then computed the normalized cross-correlation on MATLAB between miniCic intensity and the smooth of the cell elimination function (smooth window 29) and averaged cross-correlation curves for every square of analysis.

Notum wounding was performed as described previously [9], using exposure at full power with an Argon laser (488 and 458nm) and a 405nm diode in the wounded region over 3min. For experiment in Figures 5J and 5K, tissue square dissection was performed using a pulsed 355nm laser (Teem photonics, 20kHz, peak power 0.7kW) controlled by the ILas pulse system (Gataca systems) on an inverted Nikon eclipse Ti2 microscope (plan fluor 40X 1.3 N.A, oil) equipped with a Yokogawa CSU-W1 spinning disc system and a prime95 sCMOS camera (Photometrics). The region of ablation was a 400x400px square (110x110 μm) with a band of 10px width and 10 repetitions (AOTF 35%). Relaxation was imaged using z-acquisitions in green and red channels every 2min combined with an autofocus between each time point. Images shown are local z-projections. Quantification of cell area was performed in Tissue analyzer [62], intensity of miniCic was quantified after tissue drift correction (Fiji plugin StackReg), bleaching correction (on the full movie) and removal of the background (rolling ball radius 50px).

For Figure 6, PIV analysis was performed as described previously [9], using MatPIV toolbox on MATLAB with 64px windows with 50% overlap and a rolling window of time averaging of 9 frames. Compaction rate is defined as ''- *Divergence''* of the vector field (calculated on MATLAB). Averaged compaction rates were calculated by averaging on one PIV window the compaction rate over the full movie (700 min). The same squares were used to quantify miniCic signal at the last time point of the movie excluding any zone that partially overlapped with the Ras clones. The mean miniCic signal was then calculated for each bin of compaction rate values and the full dataset was used to calculate a Pearson correlation coefficient.

QUANTIFICATION AND STATISTICAL ANALYSIS

Data were not analyzed blindly. No specific method was used to predetermine the number of samples. The definition of n and the number of samples is given in each figure legend and in the table of the Experimental Model and Subject Details section. Error

bars are standard error of the mean (s.e.m.). p values are calculated through t test if the data passed normality test (Shapiro-Wilk test), or Mann-Whitney test if the distribution were not normal. For proportion (death probability), the error bars are 95% confidence interval and p value are calculated through a Fisher exact test. Statistical tests were performed on Graphpad Prism 8.

DATA AND SOFTWARE AVAILABILITY

The custom made adaptive local z-projection procedure was written on MATLAB. Basically it uses a reference channel (here E-cad::GFP) to find locally the plane of focus and perform a local projection around this plane of reference for a second channel. The code can be found in the Supplemental information (Methods S1). The principle is explained in the Method Details section.

Current Biology, Volume *29*

Supplemental Information

Competition for Space Induces Cell Elimination through Compaction-Driven ERK Downregulation

Eduardo Moreno, Léo Valon, Florence Levillayer, and Romain Levayer

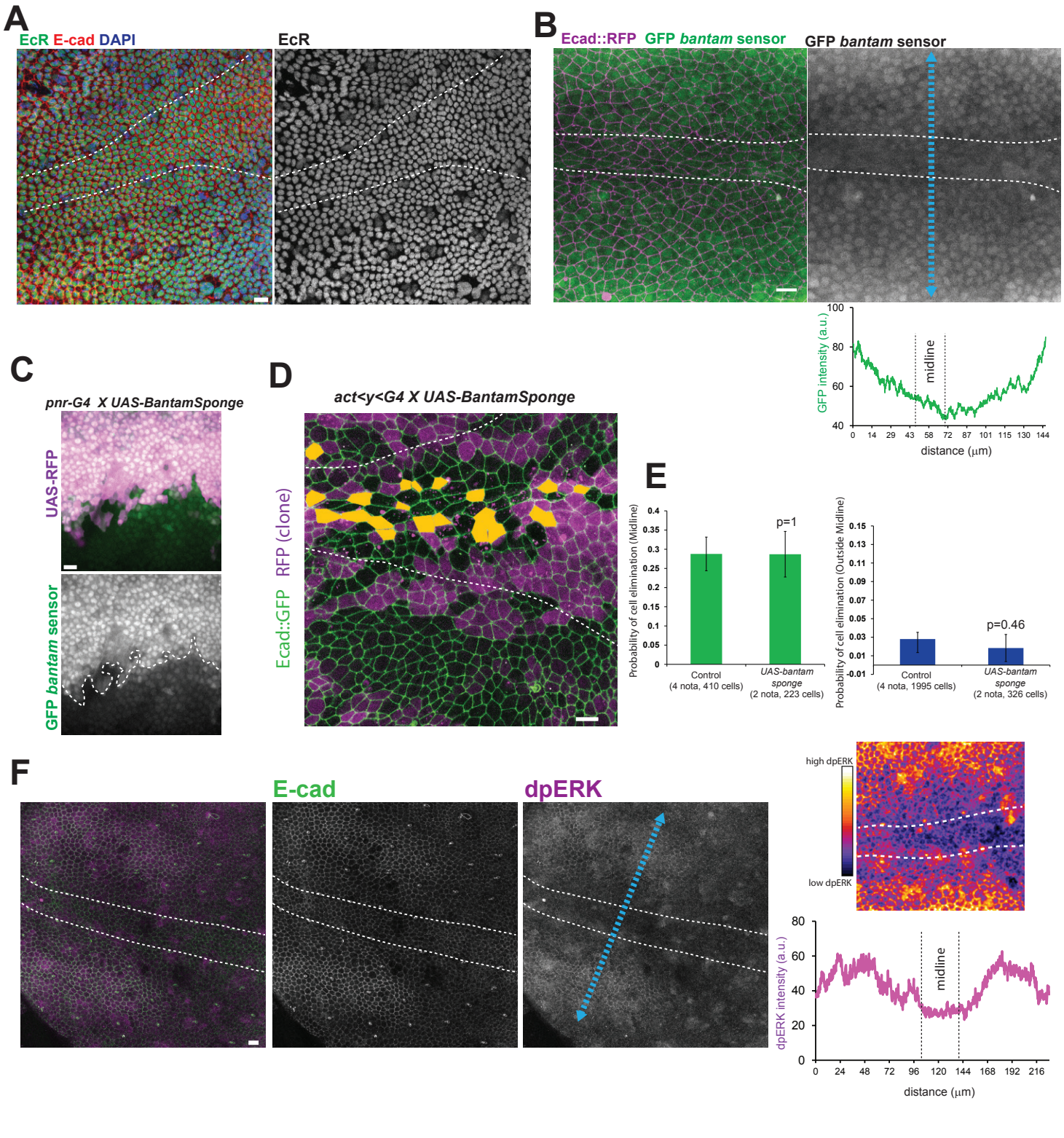
A
EcR E-cad DAPI
EcR
B
Ecad::RFP GFP bantam sensor
GFP bantam sensor
GFP intensity (a.u.)
midline
distance (μm)
C
pnr-G4 X UAS-BantamSponge
UAS-RFP
GFP bantam sensor
D
act<y<G4 X UAS-BantamSponge
Ecad::GFP RFP (clone)
E
Probability of cell elimination (Midline)
p=1
Control
(4 nota, 410 cells)
UAS-bantam sponge
(2 nota, 223 cells)
Probability of cell elimination (Outside Midline)
p=0.46
Control
(4 nota, 1995 cells)
UAS-bantam sponge
(2 nota, 326 cells)
F
E-cad
dpERK
high dpERK
low dpERK
dpERK intensity (a.u.)
midline
distance (μm)

Figure S1. Bantam and Ecdysone are not responsible for cell death in the midline. Related to Figure 2 and Video S1.

A: z-projection of an immunostained pupal notum for Ecdysone receptor (EcR, green), DAPI (blue) and GFP (for E-cad::GFP, red). The midline is encompassed by the dashed lines. Scale bar=10 μm. **B:** z-projection of a live pupal notum expressing ubi-Ecad::RFP (magenta) and a GFP *bantam* sensor (green, low GFP= high *bantam*), midline region marked by white dashed lines. Intensity profile of the GFP along the blue line is shown below. Scale bar=10 μm. **C:** z-projection from a live pupal notum expressing UAS-BantamSponge and a RFP in the *pnr* domain (magenta) and the GFP bantam sensor (bottom). GFP accumulates in the *pnr* domain compared to more lateral domains, suggesting that Bantam activity is indeed reduced by the sponge. Scale bar=10 μm. **D:** z-projection of live a pupal notum expressing *ubi-Ecad::GFP* (green) with Gal4 expressing clones (RFP, magenta) expressing a *bantam* sponge. The midline is delineated by white dashed lines. Orange cells are the clonal cells that will die over the course of the movie (700 min). See **Figure 1C** for control. Scale bar=10 μm. **E:** Quantification of the probability of cell elimination in the clones in the midline region (left) and outside the midline region (right). p-values are Fisher exact tests with the control condition (same as **Figure 1C,D**). **F:** z-projection of an immunostained pupal notum for E-cad (green) and dpERK (magenta, right panel shows a higher magnification in pseudocolours). The midline is encompassed by the dashed lines. Scale bar=10 μm. Intensity profile of dpERK along the blue line is shown on the right.

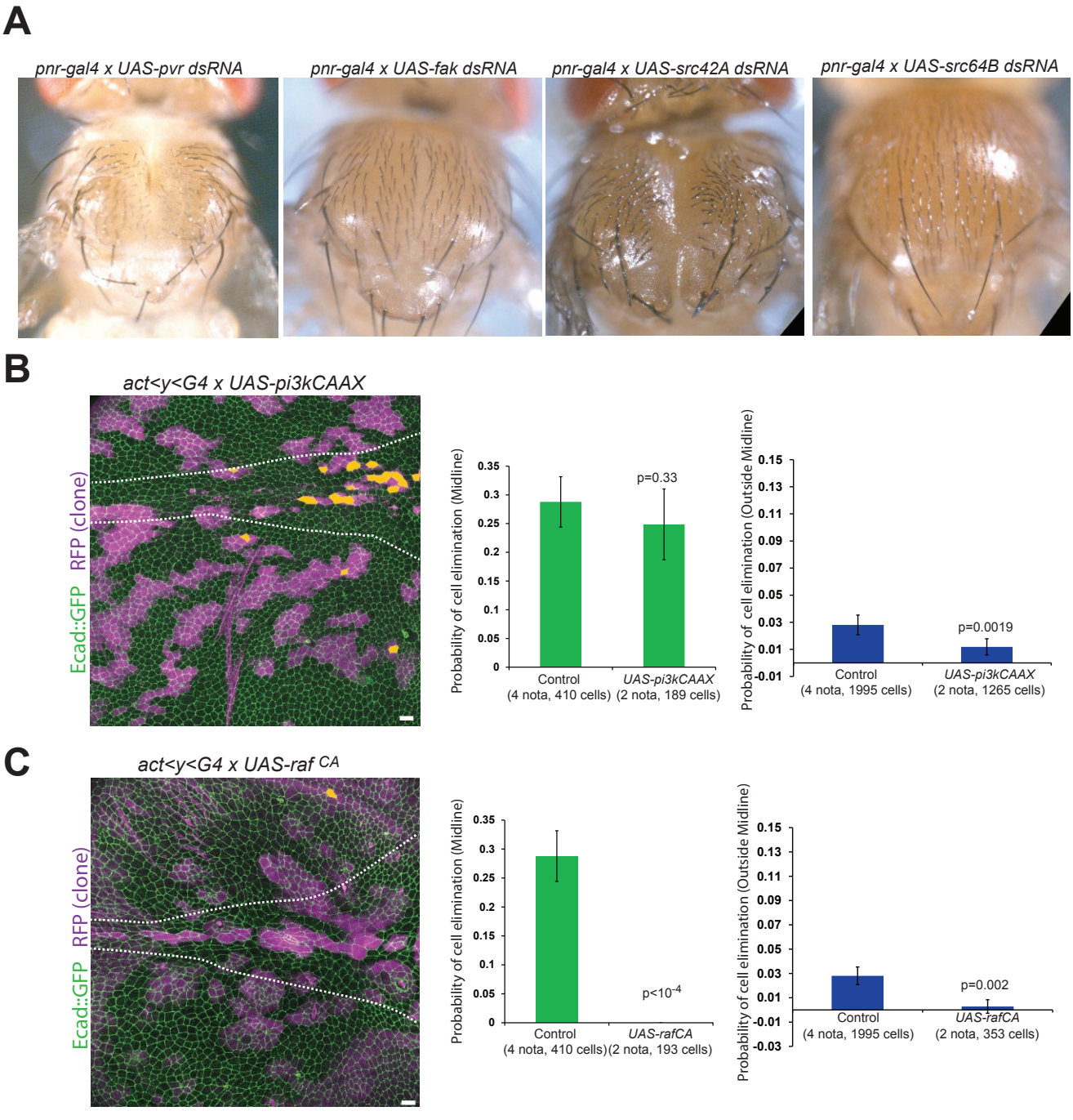
A
pnr-gal4 x UAS-pvr dsRNA
pnr-gal4 x UAS-fak dsRNA
pnr-gal4 x UAS-src42A dsRNA
pnr-gal4 x UAS-src64B dsRNA
B
act<y<G4 x UAS-pi3kCAAX
Ecad::GFP RFP (clone)
Probability of cell elimination (Midline)
p=0.33
Control
(4 nota, 410 cells)
UAS-pi3kCAAX
(2 nota, 189 cells)
Probability of cell elimination (Outside Midline)
p=0.0019
Control
(4 nota, 1995 cells)
UAS-pi3kCAAX
(2 nota, 1265 cells)
C
act<y<G4 x UAS-raf CA
Ecad::GFP RFP (clone)
Probability of cell elimination (Midline)
p<10-4
Control
(4 nota, 410 cells)
UAS-rafCA
(2 nota, 193 cells)
Probability of cell elimination (Outside Midline)
p=0.002
Control
(4 nota, 1995 cells)
UAS-rafCA
(2 nota, 353 cells)

Figure S2. Cell survival is regulated by Raf, not PI3K, PVR, FAK, Src42A or Src64B. Related to Figure 2 and Video S1.

A: Representative adult thoraxes upon PVR, FAK, Src42A or Src64B downregulation by RNAi using the *pnr-gal4* driver. Compare with **Figure 1B** (*UAS-lacZ*) for control (minimum of 10 thorax per condition). **B,C** z-projection of live pupal nota expressing *ubi-Ecad::GFP* (green) with Gal4 expressing clones (RFP, magenta) expressing active PI3K (*UAS-pi3kCAAX*, top) or active Raf (*UAS-raf*^{CA}, bottom). The midline is delineated by white dashed lines. Orange cells are the clonal cells that will die over the course of the movie (700 min). See **Figure 1C** for control. Scale bars=10 μm. Right: Quantification of the probability of cell elimination in the clones in the midline region (left, green) and outside the midline region (right, blue). p-values are Fisher exact tests with the control condition (same as **Figure 1C,D**). Note that we previously showed the efficiency of PI3K pathway activation upon *pi3kCAAX* expression exactly in the same condition previously [S1].

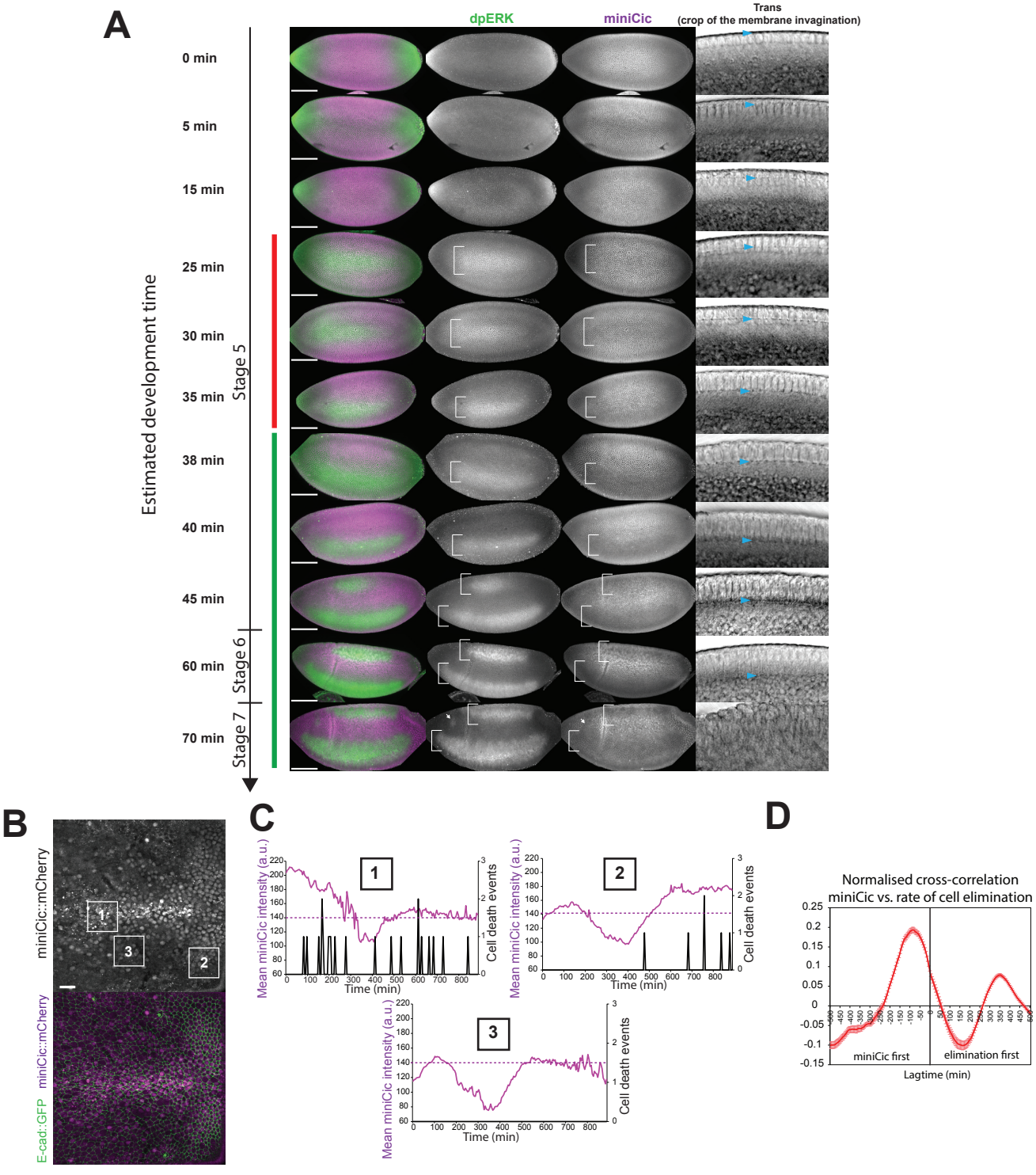
A
dpERK
miniCic
Trans
(crop of the membrane invagination)
Estimated development time
0 min
5 min
15 min
25 min
30 min
35 min
38 min
40 min
45 min
60 min
70 min
Stage 5
Stage 6
Stage 7
B
miniCic::mCherry
E-cad::GFP
C
Mean miniCic intensity (a.u.)
Cell death events
Time (min)
D
Normalised cross-correlation
miniCic vs. rate of cell elimination
miniCic first
elimination first
Lagtime (min)

Figure S3. miniCic in embryos and correlation between miniCic and cell elimination in the notum. Related to Figure 3.

A: z-projections of immunostained embryos at the cellularising (stage 5) and early gastrulating stage (stage 6,7). dpERK in green, anti mCherry (for miniCic::mCherry) in magenta. Development time (after onset of cellularisation) is estimated by the size of the invaginating membranes (transmission light, right panels, close up view of the ventral side of the embryo, blue arrowheads show the membrane front) compared to movies of cellularising embryos (not shown). White brackets show the ventral lateral zone of activation of ERK and the dorsal zone of activation. The red bar shows the first stages of dpERK activation where there is no obvious local downregulation of miniCic. At later stages, the dpERK pattern is well reflected by the absence of nuclear miniCic (brackets and white arrows). Scale bars=100 μm. **B:** Local projection of miniCic (greyscale and purple) and E-cad::GFP (green from a pupal notum at 14hAPF, from **Figure 3F**). Scale bar=20 μm. **C:** Evolution of miniCic mean intensity in the three white square regions (**Figure S3B**, 1: midline, 2: posterior region, 3: lateral region) and counting of cell elimination events in the same regions (one peak=complete removal of the cell from the epithelial plane). Purple doted lines show the mean intensity from regions with no accumulation of miniCic in the nucleus. **D:** Averaged cross-correlation between miniCic intensity and rate of cell elimination of the corresponding pupae for 54 subregions, error bars are s.e.m..

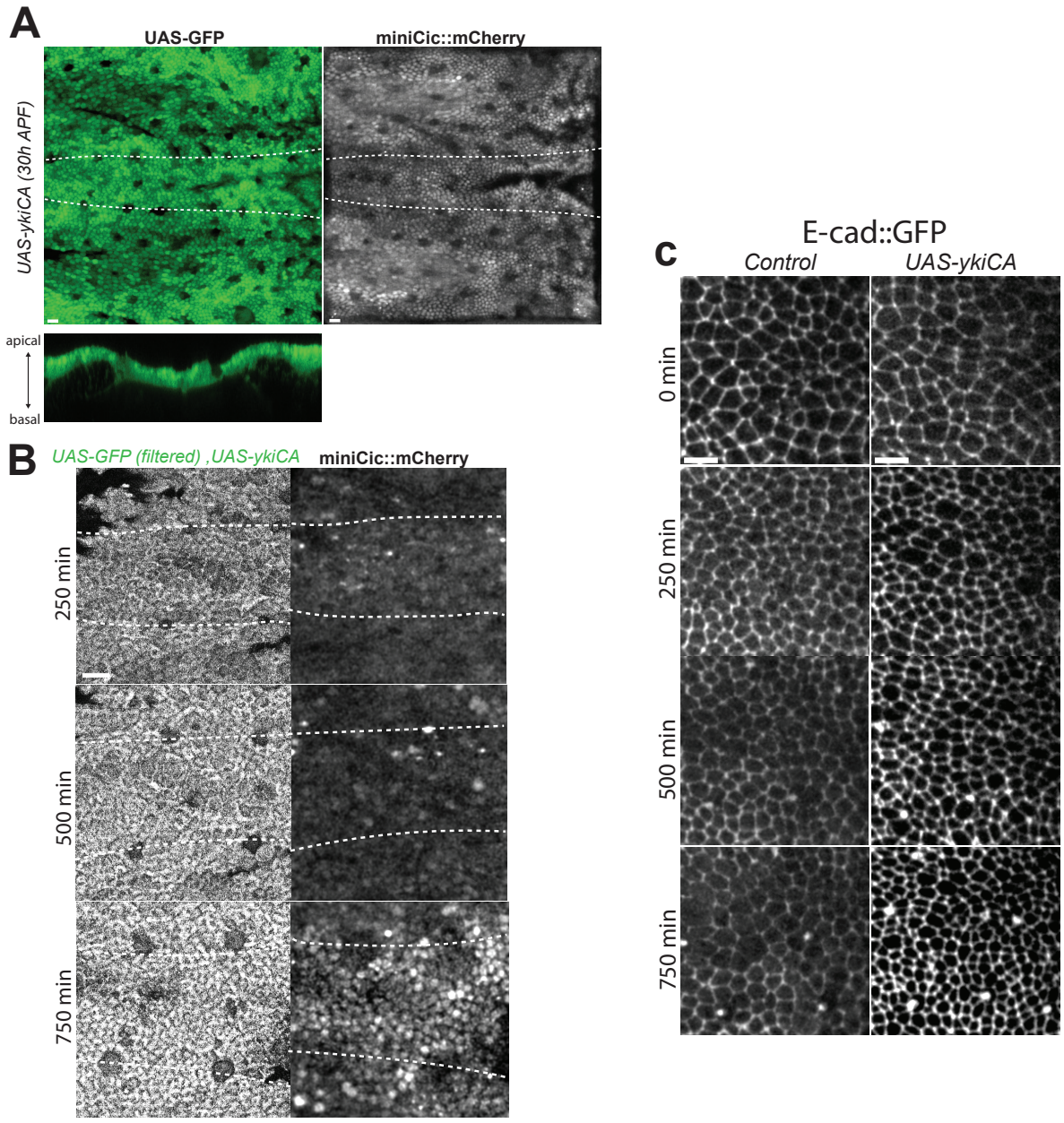
A
UAS-GFP
miniCic::mCherry
UAS-ykiCA (30h APF)
apical
basal
B
UAS-GFP (filtered) ,UAS-ykiCA
miniCic::mCherry
250 min
500 min
750 min
c
E-cad::GFP
Control
UAS-ykiCA
0 min
250 min
500 min
750 min

Figure S4. ERK is downregulated upon Yki activation in the notum. Related to Figure 5.

A: Local projection of miniCic signal (right) in a 30h APF notum upon conditional activation of Yki in large clones (*UAS-ykiCA*, GFP, green) (representative of 10 pupae). Note the global downregulation of ERK in the tissue (compare with **Figure 3F** right panel). Cell proliferation induces the formation of large folds in the tissue (see lateral section of GFP, bottom inset). Scale bar=10 μm. **B:** Snapshots of the midline (white doted lines) at different times upon induction of Yki^{CA} (GFP, filtered for the local projection, top) showing miniCic evolution (local projection, bottom). Scale bar=10 μm. **C:** z-projection of E-cad::GFP at different times in control (left, *UAS-lacZ*) and upon induction of Yki^{CA} (right) from the same region in the notum (in between midline and aDC and pDC macrochaetes) showing the increase of cell density upon Yki induction. Scale bars=10 μm. Note that we cannot exclude that Yki affects ERK independently of mechanics.

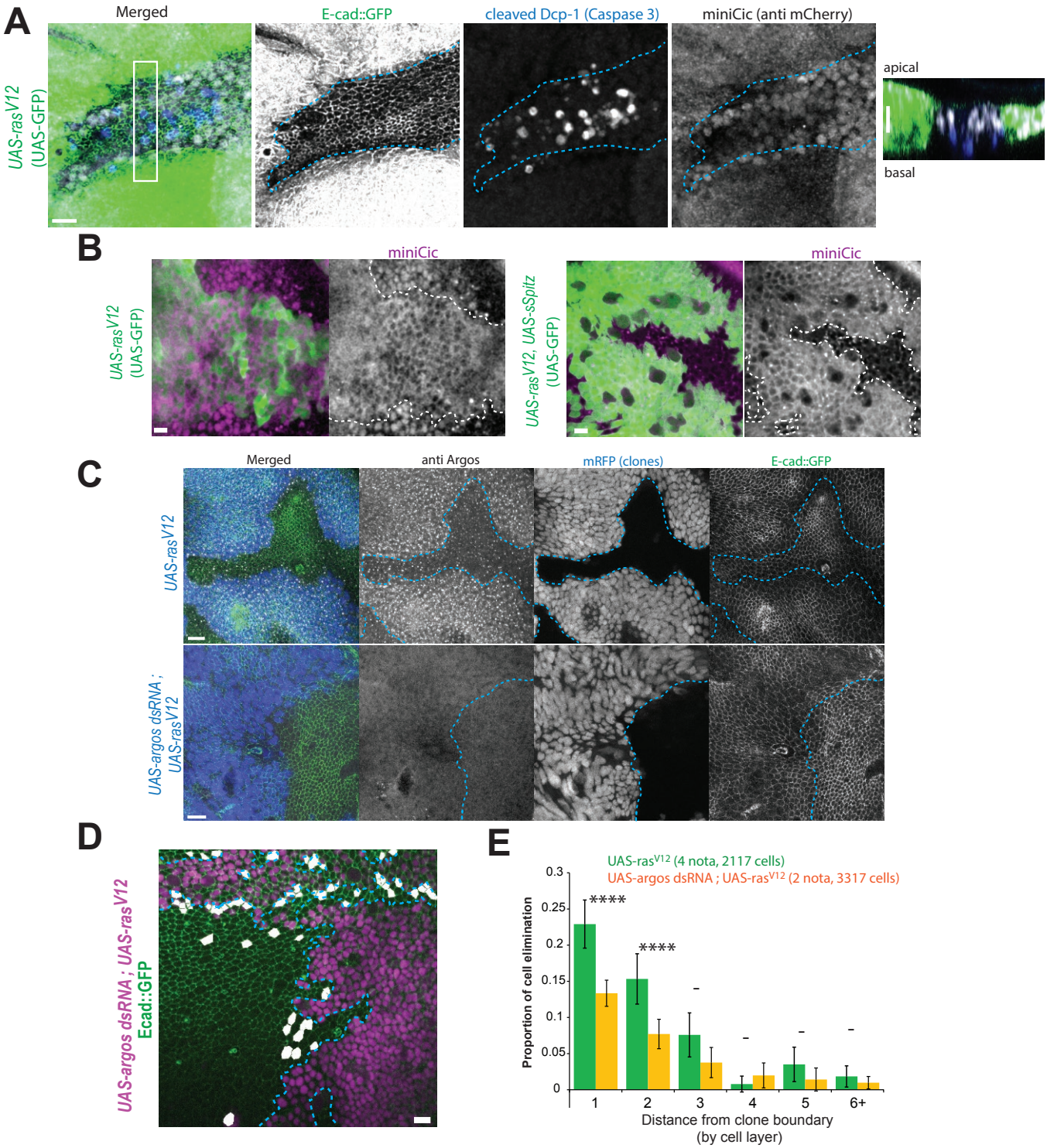
A
Merged
E-cad::GFP
cleaved Dcp-1 (Caspase 3)
miniCic (anti mCherry)
UAS-rasV12 (UAS-GFP)
apical
basal
B
miniCic
UAS-rasV12 (UAS-GFP)
UAS-rasV12, UAS-sSpitz (UAS-GFP)
C
Merged
anti Argos
mRFP (clones)
E-cad::GFP
UAS-rasV12
UAS-argos dsRNA ; UAS-rasV12
D
UAS-argos dsRNA ; UAS-rasV12
Ecad::GFP
E
UAS-rasV12 (4 nota, 2117 cells)
UAS-argos dsRNA ; UAS-rasV12 (2 nota, 3317 cells)
Proportion of cell elimination
0.3
0.25
0.2
0.15
0.1
0.05
0
****
****
1
2
3
4
5
6+
Distance from clone boundary
(by cell layer)

Figure S5. Cell elimination near Ras activated clones is not purely Argos dependent. Related to Figure 6 and Video S4.

A: z-projection in the notum near activated Ras clones (Green, UAS-GFP) showing apoptotic WT cells (blue, cleaved Dcp-1) in the region of low ERK activity (accumulation of nuclear miniCic). Blue doted lines show clone contours. Right panel shows the lateral section marked with the white rectangle. Scale bars=10 μm. **B:** Single plane view from live pupae of miniCic signal (purple and greyscale) near activated Ras clones (Green, left, white doted lines) and activated Ras clones expressing secreted Spitz (Green, right, white doted lines). In both conditions, ERK is still activated in the clones, however we don't observe anymore ERK downregulation in the neighbouring cells upon Spitz secretion (6 pupae). **C:** z-projection in E-cad::GFP (green) nota near clones overexpressing active Ras (*UAS-ras^{V12}*, blue=UAS-mRFP, top) or active Ras and a dsRNA targeting Argos (*UAS-argos dsRNA; UAS-ras^{V12}*, blue=UAS-mRFP, bottom) stained for Argos (grey) 24h after activation at 29°C. Blue doted lines show clone contours. Argos accumulation in active clones is lost upon dsRNA expression. Scale bars=10 μm, representative of 3 nota for each. **D:** z-projection of a live pupal notum expressing endo-Ecad::GFP (green) upon conditional induction of *Ras^{V12}* and *argos-dsRNA* in clones (RFP, strong magenta signal, blue dashed lines=clone contours). The cells that will die during the movie are shown in white. Scale bar=10 μm. **E:** Quantification of the probability of cell death for a given distance to clone boundaries (cell rows). Control (green bars) comes from **Figure 6C,D**. **** =$p<10^{-4}$, **-** =$p>0.05$, Fisher exact test with *UAS-ras^{V12}* (green bars). Although there is a diminution of the rate of elimination, there is still a strong increase of cell death near the clones (contrary to *UAS-sSpitz* or *UAS-sqhE20E21*, **Figure 6D**).

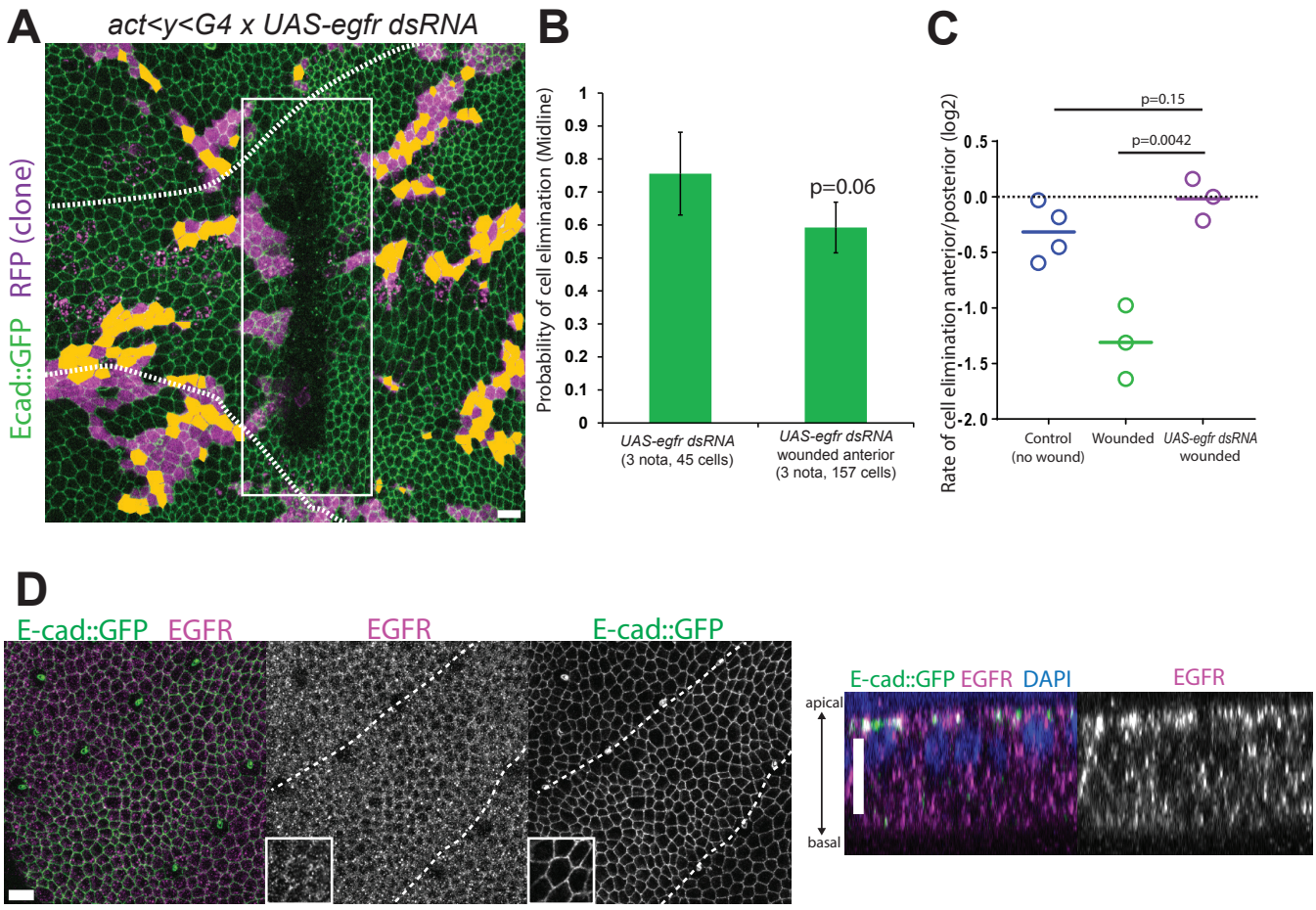
A
act<y<G4 x UAS-egfr dsRNA
Ecad::GFP RFP (clone)
B
Probability of cell elimination (Midline)
1
0.9
0.8
0.7
0.6
0.5
0.4
0.3
0.2
0.1
0
p=0.06
UAS-egfr dsRNA
(3 nota, 45 cells)
UAS-egfr dsRNA
wounded anterior
(3 nota, 157 cells)
C
Rate of cell elimination anterior/posterior (log2)
p=0.15
p=0.0042
0.5
0.0
-0.5
-1.0
-1.5
-2.0
Control
(no wound)
Wounded
UAS-egfr dsRNA
wounded
D
E-cad::GFP EGFR
EGFR
E-cad::GFP
E-cad::GFP EGFR DAPI
EGFR
apical
basal

Figure S6. Mechanical sensitivity of ERK pathway is upstream and/or at the level of EGFR. Related to Figure 6, Discussion and Video S5.

A: z-projection of a live pupal notum expressing *ubi-Ecad::GFP* (green) with Gal4 expressing clones (RFP, magenta) where EGFR is downregulated (*UAS-egfr dsRNA*) after laser wounding (white rectangle, anterior on the left side, posterior on the right). The midline is delineated by white dashed lines. Orange cells are the clonal cells that will die over the course of the movie (700 min). Scale bar= 10μm. **B:** Quantification of the probability of cell elimination in the *UAS-egfr dsRNA* clones in the midline region without wounding (from **Figure 2C,D**), or upon wounding in stretched clones anterior to the wound. p-value is Fisher exact test. **C:** Quantification of the relative rate of cell extrusion in the midline region anterior and posterior to the wound in controls (no wounding), upon wounding (middle), and in wounded nota after depletion of EGFR in clones. One circle=one notum. Note that the data for the Control and Wounded are coming from [S2]. While wounding normally induced a reduction of cell elimination anterior to the wound relative to the posterior region (since cell stretching is induced anterior to the wound because of the global tissue flow), there was however no apparent difference in the rate of cell elimination anterior and posterior to the wound in EGFR depleted clones (see p-values, t-tests). This was suggesting that EGFR depleted clones were insensitive to stretching, suggesting that stretching acts at the level or upstream of EGFR. **D:** Z-projection of a pupal notum stained for EGFR (purple) and E-cad::GFP (green) in the midline (white doted lines), representative of 5/5 pupae. Note the apical and cortical pool of EGFR (see insets). Lateral view of EGFR, E-cad::GFP and DAPI (blue) shown on the right side. Scale bars= 10μm.

Supplemental References

S1. Levayer, R., Hauert, B., and Moreno, E. (2015). Cell mixing induced by myc is required for competitive tissue invasion and destruction. Nature *524*, 476-480.

S2. Levayer, R., Dupont, C., and Moreno, E. (2016). Tissue Crowding Induces Caspase-Dependent Competition for Space. Curr Biol *26*, 670-677.